Chapter 2

Stereology and Its Application to Pathology

In the examples of morphometry shown in the foregoing chapter, we were able to reach a conclusion only through measurements on 2-D pictures. There was no need to take into consideration the 3-D structure of objects. However, often we are required to obtain information about the 3-D structure.

We pathologists always make diagnosis based on observation of pictures, including macroscopic, microscopic and electron microscopic pictures. However, available for us are almost always 2-dimensional (2-D) pictures, or sections. A microscopic picture is of course a sectional one, and so is an electron micrograph. Also, a cut surface of an organ is another example of 2-D picture. However, they are all sections of what in itself is a 3-D structure. It seems that while looking at a 2-D microscopic section, we are always trying to understand, even if not being aware, what 3-D structure such a section may have been generated from. Often this attempt fails and ends up in confusion, particularly when we are dealing with a complicated one. On such occasions, some of us may attempt at resorting to 3-D reconstruction from serial sections, a time-honored technique of morphology long used in pathology and microanatomy. However, this will not be undertaken very often even when it is necessary. Reconstruction is a demanding task which may cost a pathologist a great deal of time and labor.

On the other hand, efforts have been paid to establish theoretical methods to obtain information about the 3-D properties of objects, quantitative or qualitative, thereby avoiding the laborious reconstruction. As a famous and successful example one can introduce the method to estimate the surface area of the alveolar septa contained in the human lung. Weibel (1963) gave an estimate of 120 m^2 for the total alveolar surface area of both lungs combined together, and this has been considered a good one. Apparently this is a 3-D quantity which is a very important factor in correlating the structural changes of lung with its function. For example, one can expect the alveolar surface area to be much reduced in lungs with advanced emphysema, and this helps correlate the functional abnormalities of emphysematous lungs with their structural changes. Of course it is not practicable to separate the lung tissue to pieces and directly measure the surface area of fragments. In fact, the quantity was estimated indirectly from microscopic measurement on 2-D lung sections, relying on a mathematical principle. Here we find a “bright” technique allowing us to know about the three dimensions without making direct access with serial sections. There are also other principles and technique we can apply in estimating 3-D quantities from measurements on 2-D sections. To such methodology, a generic term has been given: stereol-

ogy, the science of 3-D (Bach, 1963).

Of the various methods of stereology developed, some basic principles are to be introduced here, together with examples of their application:

the volume ratio of a structural component (V_V: volume density)
the surface area in a unit volume (S_V: surface area density)
the total length in a unit volume (L_V: length density in space)
stereology of particles (granulometry).

a) Evaluation of paraquat-induced atelectasis

Hamster lung in experimental paraquat toxicity (Figs. 2-1, 2-2)

Paraquat (1,1'-dimethyl-4, 4'-bipyridylium chloride), a herbicide widely used in Japan, has been the prime cause of fatal intoxication after ingestion, whether accidental or with suicidal intent. In fatal cases of intoxication, severe respiratory distress emerges on the fourth or fifth day and the condition of the subject rapidly deteriorates (Smith *et al*., 1974). At autopsy, lungs are confirmed to be the main site of fatal changes, ranging from diffuse alveolar damage to dense fibrosis. In an experimental attempt at visualizing the earliest changes of lung, hamsters were given a small amount of paraquat intraperitoneally. Figure 2-1 is a microscopic section of lung 30 minutes after the administration where, as yet, no paraquat-related changes have emerged. The image contains a terminal bronchiole, respiratory bronchioles, alveolar ducts and many alveoli, with their air spaces fully open and with all the alveoli unfolded. Figure 2-2

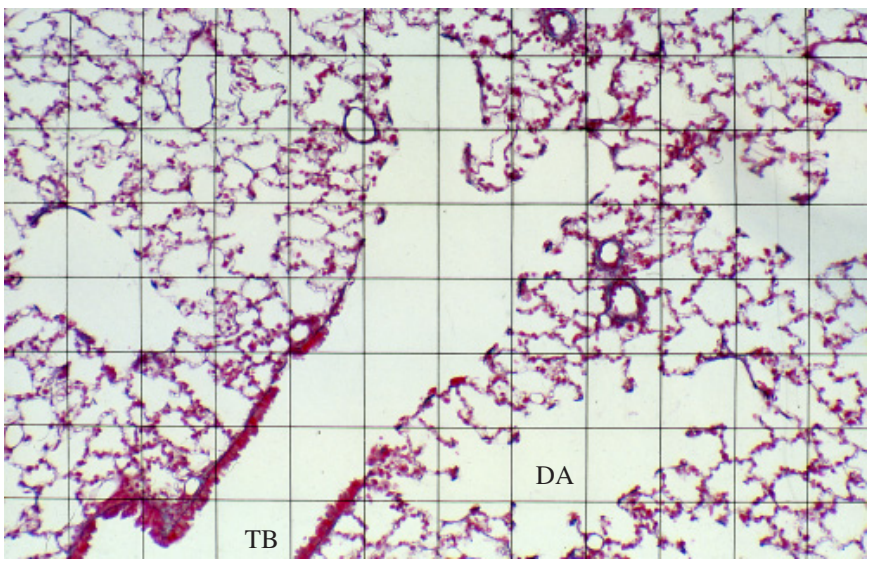

Fig. 2-1. Estimation of areal ratio for ductus alveolaris (DA) and terminal bronchiole (TB) by point counting, in a lung of hamster 30 minutes after paraquat was given, still retaining the normal structure. The cross points of the overlaid grid serve as sampling points. The areal ratio of DA combined with TB (20/77) can directly be interpreted as their volume ratio. Elastica-Goldner stain.

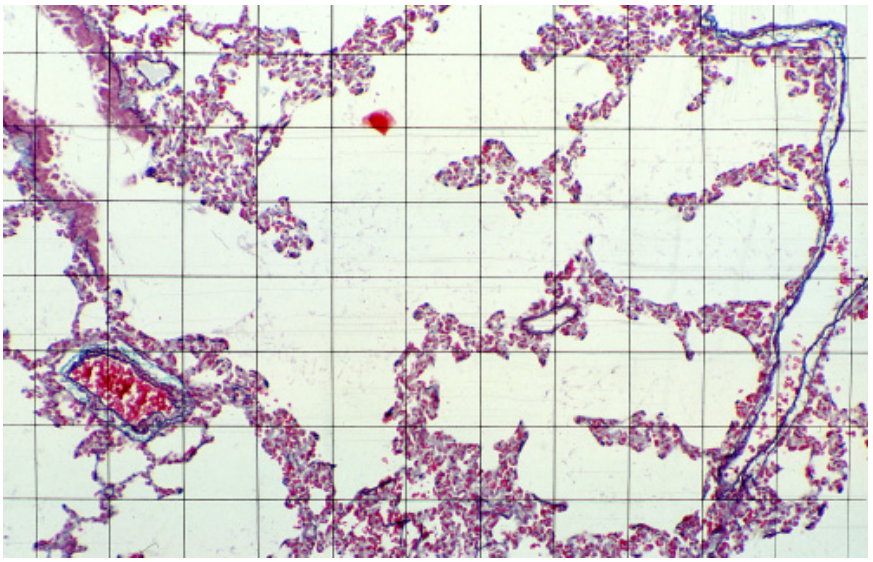

Fig. 2-2. Point counting in a hamster lung in early paraquat toxicity, 24 hours after administration. The alveolar ducts are strongly dilated, as demonstrated by the areal (volume) ratio that is elevated to 44/84 = 0.524. The alveoli are all collapsed in a state of alveolar atelectasis. Elastica-Goldner stain.

demonstrates the state of lung 24 hours after the administration. Here the individual alveoli have lost aeration, with the septa closely adherent one to another, showing a change called alveolar atelectasis; instead, however, the alveolar ducts are all strongly dilated. Both of the lungs were carefully fixed so as to keep the *in vivo* state of aeration as faithfully as possible; they were kept in fixative and aspirated from exterior by connecting the air-tight container with a water-jet pump. The difference in the volume share of alveolar ducts and other parts of bronchiolo-alveolar system was compared between the two conditions with V_V(ad), the volume of alveolar ducts (including the terminal bronchioles) in a unit volume, or the volume density.

Look at the grid of "tessellated" type with vertically crossing parallel lines that is overlaid upon the microscopic pictures. In practice, we use an eyepiece bearing the grid pattern which is put in an ocular lens of microscope (Fig. 2-4 upper). Figure 2-1 contains 77 crossing points of lines and Fig. 2-2 contains 84, and we can find some of the points hitting, for example, air spaces in the alveolar ducts. In Fig. 2-1 we count the number of points hitting the alveolar ducts (and terminal bronchioles), and obtain a result of 20 points. Then, the fraction of area occupied by the air space of alveolar ducts A_A(ad) on section is estimated to be approximately 20/77 = 0.260. According to one of the basic principles of stereology,

$$V_V \doteqdot A_A \tag{2-1}$$

which means that the volume ratio of a component in a 3-D structure (V_V) is approximated with its areal ratio (A_A) on a random 2-D section of the structure. Therefore in

this case, we can regard the air space fraction of alveolar ducts V_V(ad) also as about 26.0%. The measurement was extended to Fig. 2-2, and here we see 44 of 84 points hitting the spaces of alveolar ducts, showing that V_V(ad) has been increased into 44/84 = 0.524. Similarly, the air space fraction for alveoli V_V(al) in Fig. 2-1 is shown to be about 49/77 = 0.636 while in Fig. 2-2, it is reduced to 26/84 = 0.310. All these may be interpreted as suggesting that the alveolar septa are stuck one to another, causing a state of alveolar collapse, suggesting that the lung as a whole has lost its extensibility. This is a state of alveolar atelectasis which is attributable to surfactant deficiency caused by paraquat-induced injuries to Type II pneumocytes, the main producer of surface active agents. In fact, in the lungs of hamsters in the state of Fig. 2-2, clear signs of injury in Type II cells were confirmed electron microscopically.

There are several methods to measure the area of the structure of interest in a section. If a semi-automatic digital image processor is available, it may prove to be helpful. However, the "point counting" technique shown above is the easiest to practice and therefore used worldwide. If microphotographs are used as material, one can perform point counting by overlaying the photograph with a plastic sheet printed with tessellated grid, instead of using an eyepiece.

Point counting vs. chord length measurement for V_V (Figs. 2-3, 2-4)

There is another method of estimating V_V on section instead of point counting. Figure 2-3 is meant to show a sectional picture of carcinoma where the areal ratio A_A is to be determined for either the carcinoma cell nests, or the interstitium. Of course,

$$A_A \text{ (cell nests)} + A_A \text{ (interstitium)} = 1.0$$

In the upper figure, point counting is performed, with the nests occupying 20/63 points, or A_A(nests) = 0.32. An alternative is shown in the lower figure, and here we put parallel sampling lines drawn randomly on the sectional picture. If the area of the section (or the total length of the lines) is sufficiently large, the lines come to traverse the carcinoma cell nests many times, and at each transection, generate a linear intercept, or a chord, of various length λ. If we measure λ_i for hundreds of chords that arose, A_A is estimated by

$$(V_V =)\ A_A \fallingdotseq \sum \lambda_i / L \qquad (2\text{-}2)$$

where L is the total length of sampling line.

Figure 2-4 demonstrates two types of eyepiece, the upper one for point counting and the lower, for chord length measurement. The lower one may look like an ordinary eyepiece widely used for microscopy, but the difference is that it has a line transversely penetrating the scales, and this serves as sampling line. While observing a sectional picture under microscope, we can extend sampling as much as necessary by moving the picture in the direction parallel to the line.

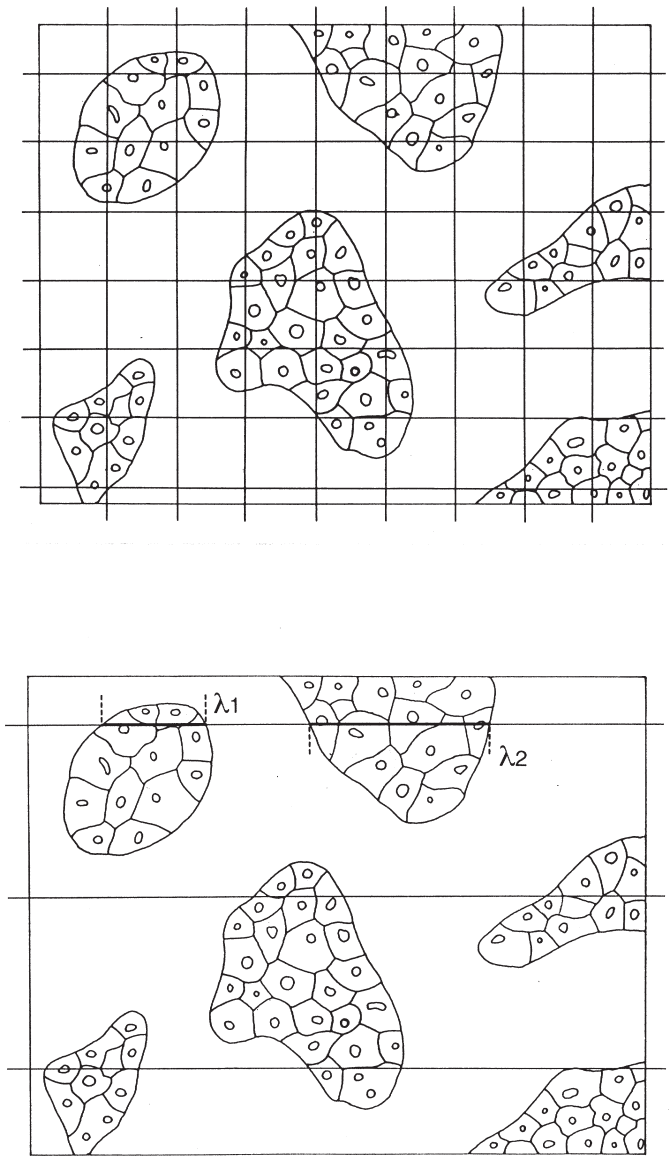

Fig. 2-3. Two methods for the estimation of V_V are schematized. Point counting (upper) vs. chord length measurement (lower) applied to carcinomatous tissue in order to determine the stromal (or parenchymal) volume ratio.

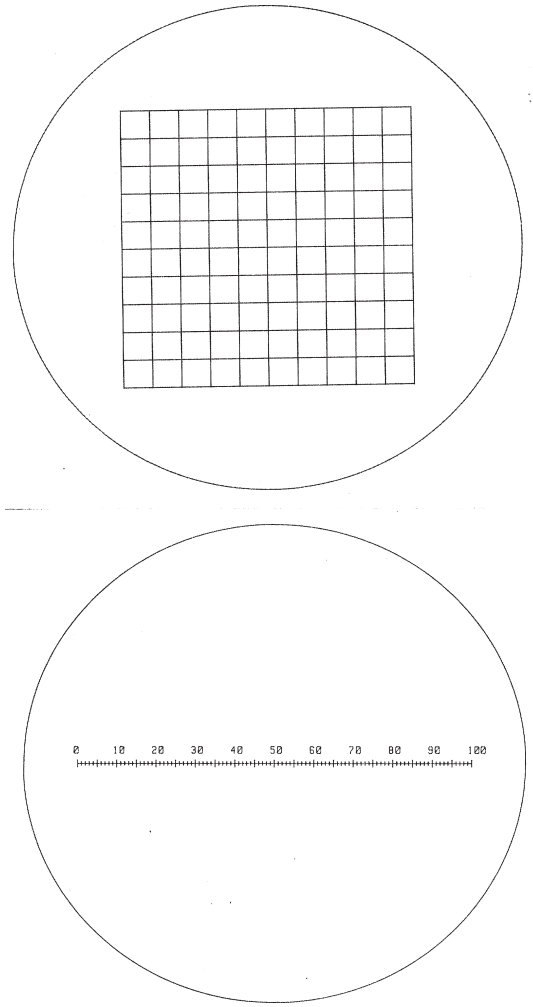

Fig. 2-4. Two types of eyepiece. Upper: "tessellated" grid which is useful in making point counting. Lower: an ocular micrometer with a line transversely penetrating the scales, convenient for chord length measurement.

b) Langerhans islets of the pancreas in diabetics

Langerhans islet of pancreas and diabetes mellitus (Fig. 2-5)

Figure 2-5 demonstrates an islet of Langerhans found in the pancreas of a non-diabetic subject. Millions of such micro-organs are dispersed in a normal pancreas of human. An islet comprises several sorts of cells, each assigned to secrete one of the islet hormones: insulin, glucagon, etc. Of the diseases associated with abnormal islet function, it is diabetes mellitus that in developed countries affects a significant and increasing part of population, raising a serious health problem.

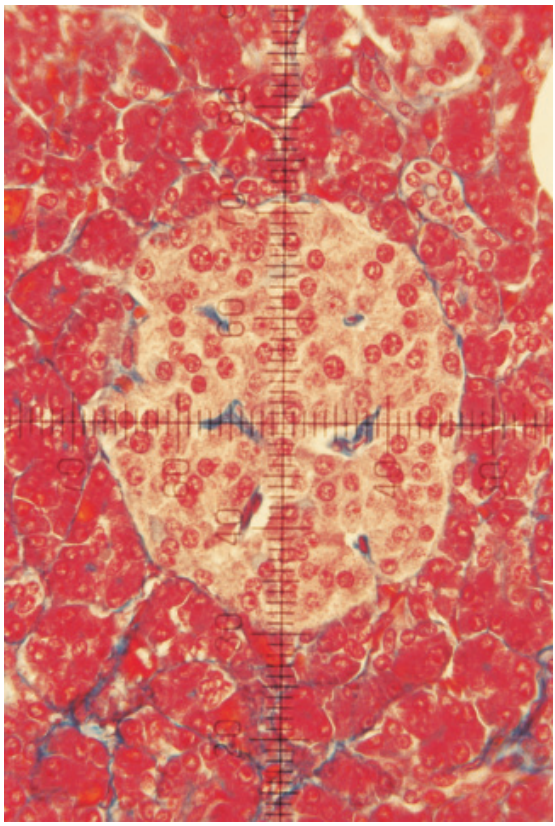

Fig. 2-5. The microscopic picture of a normal islet of pancreas. Azan-Mallory stain.

Diabetes mellitus is a metabolic disorder in which the function to metabolize carbohydrates is more or less impaired. This has been attributed to faulty activity of insulin that is secreted by what is called B cells of islets, resulting in hyperglycemia and glycosuria. There are several complications of diabetes which are often fatal and clinically more important than the metabolic disorder itself, including lowered resistance to pyogenic infection, ischemic heart disease due to advancement of atherosclerosis, and microangiopathy leading to devastating retinopathy and nephropathy. Since diabetes is primarily associated with malfunction of insulin, it would be of profound significance to make clear whether or not there are morphological changes of islets underlying the disease. Particularly, it may be crucially important to know whether diabetes is associated with quantitive changes of islets, such as their reduced volume or number. As yet, however, quantitative study of islets is retarded, and this may be attributable to the difficulties in establishing a useful geometric model for this microorgan.

The quantitative treatment of spherical bodies dispersed in the space, or granulometry, is a classic subject of stereology. Also in mophological pathology, these sorts of problems are encountered not infrequently. One may immediately be reminded

of several examples, such as regenerative nodules of cirrhotic livers or nuclei of some kind of cells, for example hepatocytes, besides, of course, pancreatic islets. However, distribution of radius of dispersed particles has not been accessible to easy morphometric technique, and the estimation of sphere number N_V in a unit volume still remains to be one of the hardest problems of biometry. In 1976, Suwa *et al*. developed a stereological method workable if one can assume that the radius r of spherical bodies follows some distribution function. This method has practical advantage as compared with the methods introduced by Scheil (1931), Schwartz (1934) or Saltykov (1958) where no such distribution function was assumed. To be outlined in the following is an application of this algorithm by Saito *et al*. (1978, 1978) to the pancreatic islets in diabetic and non-diabetic subjects.

Chord length measurement on a model of dispersed spheres (Fig. 2-6)

The aim of this model-based quantification was to estimate the total number N_i and volume V_i of islets contained in the pancreas, and parameters of islet radius distribution, including the mean and variance of radius.

Figure 2-6 is a schema showing the geometric model we used. Here we assume that the pancreatic islets can be approximated to spheres which are of varying radius r and dispersed in the space as schematized in the figure. Suppose that the space containing spheres is sectioned with a plane. In the figure, the space is cut into a cube, and in its frontal face, a number of islets are shown emerging as circular sections of various size. This is a situation corresponding to the microscopic picture of pancreas in which circular islets are scattered. Now suppose that a sampling line is drawn randomly on

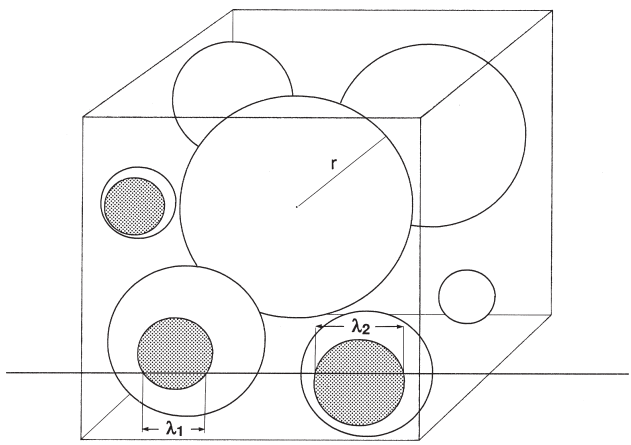

Fig. 2-6. A geometric model used for the morphometry of Langerhans islets. Islets are assimilated to spheres of different radius r and dispersed in the space. A sampling line drawn randomly on section generates a number of chords. Microscopic measurement is perfomed of the length λ for a large number of chords. Based on a stereological theorem, N_V, the number of spheres in a unit volume, the mean and variance of r are estimated from the measurements of λ.

the sectional plane. It intersects a series of circles and generates "chords" of various lengths λ. Under microscope, the length λ was measured for a number of chords, usually 200 or more, and the parameters of sample distribution for λ were obtained: N_L, the number of chords; $\sum(\lambda)_L$, the sum of λ; and $\sum(\lambda^2)_L$, the sum of λ^2, each per unit length of sampling line. Here the task is to estimate the necessary quantities about the radius r of spheres from these measurement data.

Weibull distribution assumed for sphere radius (Fig. 2-7)

As above, we assume that the sphere radius r follows a distribution function $N(r)$. Several different functions may be workable, including logarithmic normal distribution or gamma distribution, but in this study, Weibull distribution

$$N(r) = N_V m\alpha(\alpha r)^{m-1} \cdot \exp\left[-(\alpha r)^m\right] \tag{2-3}$$

was employed on account of its convenience in practical use (Fig. 2-7). The function contains three parameters. N_V is the number of spheres in a unit volume (the numerical density). The second parameter α is called the scalar because it is responsible for transformation of coordinates along the r-axis. The third, m, is the shape parameter, allowing us to obtain widely divergent shapes of distribution as the value is shifted. What a variable pattern of $N(r)$ is obtained by shifting the m-value is visualized in Fig. 2-7, where both the values of N_V and α are fixed at 1.0. It is on account of this feature that Weibull distribution finds a wide application to biological forms.

The distribution of chord length, $F(\lambda)$, is related to the distribution of $N(r)$ by the

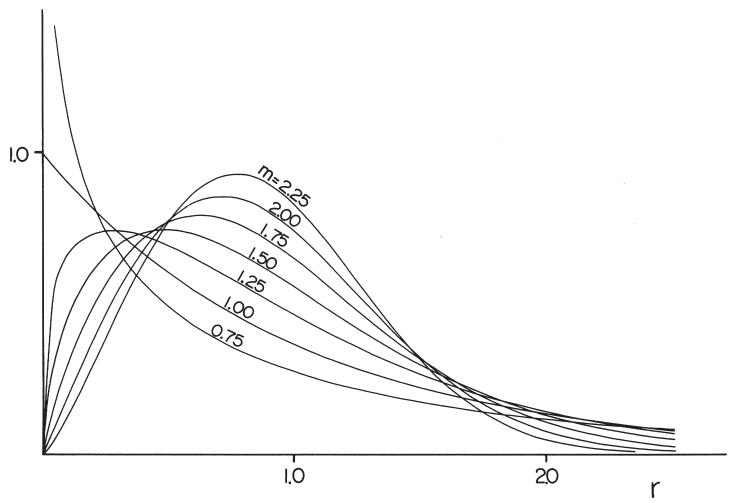

Fig. 2-7. Weibull distribution. The distribution curves with different m values. N_V and α are fixed at 1.0.

equation:

$$F(\lambda) = \frac{\pi}{2}\int_{\frac{\lambda}{2}}^{\infty} \lambda N(r)dr \tag{2-4}$$

Based on this, the parameters characterizing the distribution of r were calculated, including N_V and the mean and variance of r. For the mathematical derivation of (2-4), and also for the treatment of measurement data, see Appendix which is found at the end of this book.

Chord length λ : measurement data vs. theoretical distribution (Fig. 2-8)

Chord length λ obtained by measurement in a non-diabetic pancreas was expressed in Fig. 2-8 as a histogram. The curves entered in the figure are the theoretical $F(\lambda)$s calculated by assuming Weibull distribution, gamma distribution and logarithmic normal distribution for $N(r)$, respectively. One can see that each of the curves sufficiently agrees with the histogram, justifying to assume that r follows each of these functions.

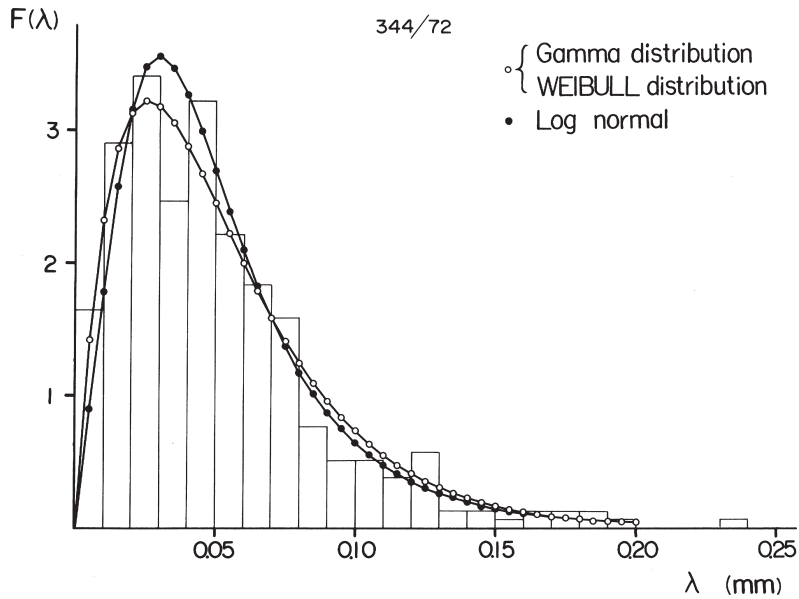

Fig. 2-8. The histogram of chord length λ generated by Langerhans islets, measured in a non-diabetic pancreas, is superimposed with the theoretical distribution assuming Weibull, gamma and logarithmic normal distributions. Each of the distributions is shown sufficiently agreeing with the histogram. Reproduced from Suwa, Takahashi *et al.* (1976): Tohoku J Exp Med 118: pp. 108.

Mean radius, total number and total volume of islets (Figs. 2-9, 2-10)

Figure 2-9 demonstrates the results of islet morphometry based on the model of dispersed spheres. The data were obtained on morphometry of pancreases taken at autopsy, all performed within 2 hours post mortem. In the upper figure, the values of mean islet radius are compared among the four groups: control non-diabetics, hypertensive non-diabetics, maturity onset (Type II) diabetics and growth-onset (Type I) diabetics. Hypertensive subjects were discriminated, considering the possibility that the islets could undergo some ischemic changes because the pancreas is one of the organs where small arteries and arterioles are particularly susceptible to hypertensive lesions. Among the four groups, one can find no significant difference in the mean islet radius. Therefore the possibility is ruled out that diabetes is associated with atrophy of islets. Shown in the lower figure are values of N_i, the total number of islets contained in the pancreas, which was obtained by multiplying N_V, the islet number in a unit volume (the numerical density of islets), by the volume of pancreas. The mean N_i for non-diabetics amounts to 8 million, but there is a notable dispersion of the estimated N_i in non-diabetic as well as in diabetic groups. Although N_i appears to be slightly smaller in maturity-onset (Type II) diabetics, the difference from the non-diabetics is not significant. Only in growth-onset (Type I) diabetics, V_i proved to be significantly lower than the other groups.

The most significant difference between the diabetics and non-diabetics was found in the total volume V_i of islets contained in the pancreas. Though there is a large within-group variation in each of the groups, the mean V_i is the highest in the non-

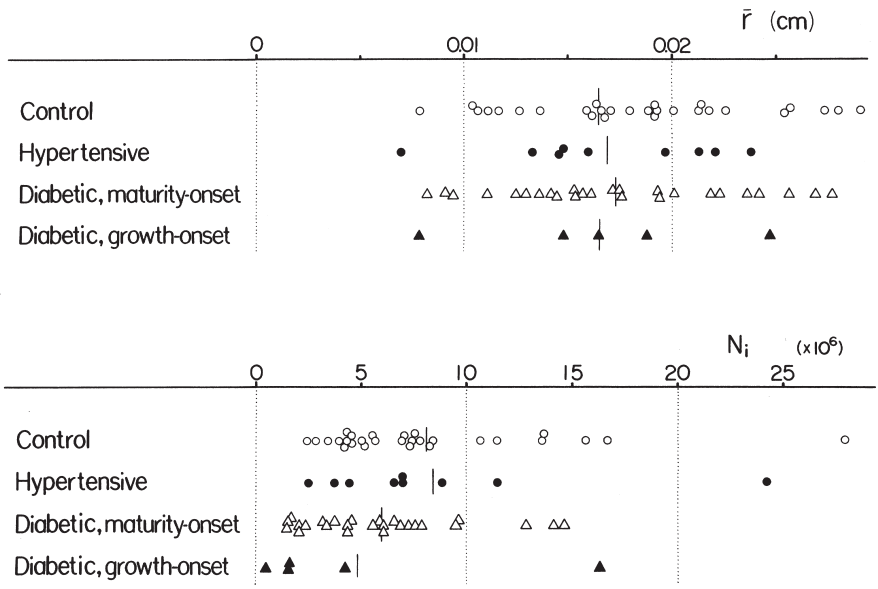

Fig. 2-9. The mean radius of islets (upper), and the total number of islets contained in the pancreas (lower), estimated stereologically. Measurement was performed on autopsy pancreases including non-diabetic non-hypertensives, non-diabetic hypertensives, maturity onset diabetics (Type II) and growth onset diabetics (Type I). Reproduced from Saito, Takahashi *et al*. (1978): Tohoku J Exp Med 125: pp.190.

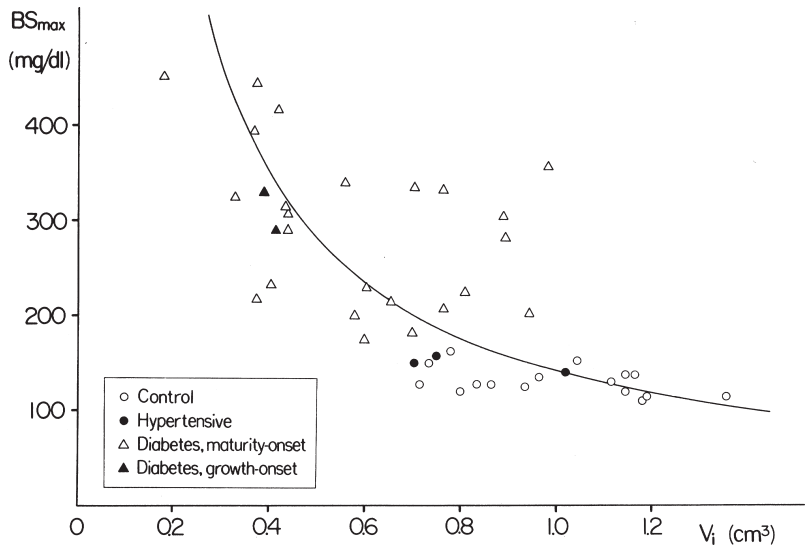

Fig. 2-10. The total islet volume V_i contained in the pancreas, correlated with the maximum blood sugar (BS_{max}) during glucose tolerance test, which is elevated in diabetics. Reproduced from Saito, Takahashi *et al.* (1978): Tohoku J Exp Med 125: pp. 193.

hypertensive non-diabetics, while it becomes smaller in the order from the hypertensive non-diabetics to maturity-onset and to growth-onset diabetics. The difference in the mean between any pair of the groups proved significant on *t*-test. In Fig. 2-10, V_i is correlated with BS_{max}, the maximum blood sugar level during glucose tolerance test (GTT), where BS_{max} during GTT increases steadily with decreasing V_i. There is a significant correlation on semi-logarithmic coordinates, showing that, of the quantitative-morphological parameters of islets, the total islet volume may serve as the best marker of glucose tolerance.

Extension to the extrainsular islet cells

An extension of this study was made by Kaiho *et al.* (1986). They extended the object of study so as to cover what had been called extrainsular islet cells, the endocrine cells dispersed in the pancreas as small clumps or even as a single cell. By this time, visualization of such minute endocrine organs had become easily practicable with the assist of immunohistochemistry. Normal pancreases obtained from three adults, taken surgically or at autopsy, were submitted to preparation of serial sections, which were immunostained for insulin. All the islets contained in a test volume (1.4 to 1.7 mm^3) were sampled, including single cell islets, and the radius r was measured under microscope for each. It was found that the distribution of r was of a strongly skewed shape, with a majority of islets having an r near to the minimum. Based on the pattern of distribution curve that was monomodal in every examined case, it was concluded that the extra-insular islet cells, though discriminated from the typical (large) islets,

belong in reality to a population common to the latter. Also, the Weibull distribution was shown to sufficiently fit the histogram of islet radius, giving support for assuming this function which has a single peak. Small islets like single cells, while accounting for a majority in the number of islets, were demonstrated to account for only a very small percentage of islet volume. It was considered that the bulk of the endocrine functions of the pancreas is carried out by large islets, whereas the extra-islet cells are likely to be their precursors.

c) Morphometry of metastatic tumor nodules in the liver

Livers with metastatic nodules: different appearance (Fig. 2-11)

Shown in the following is another example of granulometry: the quantitative treatment of metastatic tumor nodules dispersed in the liver.

Previously, it was thought that for a patient having carcinoma, for example in the large intestine, perfect cure by surgical means could hardly be expected if the patient was already confirmed to have metastasis in the liver. Recently, however, attempts are made with increasing frequency at surgical excision of the metastasis-containing part of the liver, if the part is considered removable and if a minimum life-sustaining volume of the liver can be left in a tumor-free state. In establishing a surgical strategy along this line, it would be of fundamental significance to know how many metastases a given liver can contain and at what density. Also this may be necessary in biological studies of cancer because it is often required to define, in strictly reproducible terms, to what degree a cancer is apt to generate hepatic metastasis. However, clinical imaging like CT allows to recognize only the presence of gross nodules, leaving the matter to

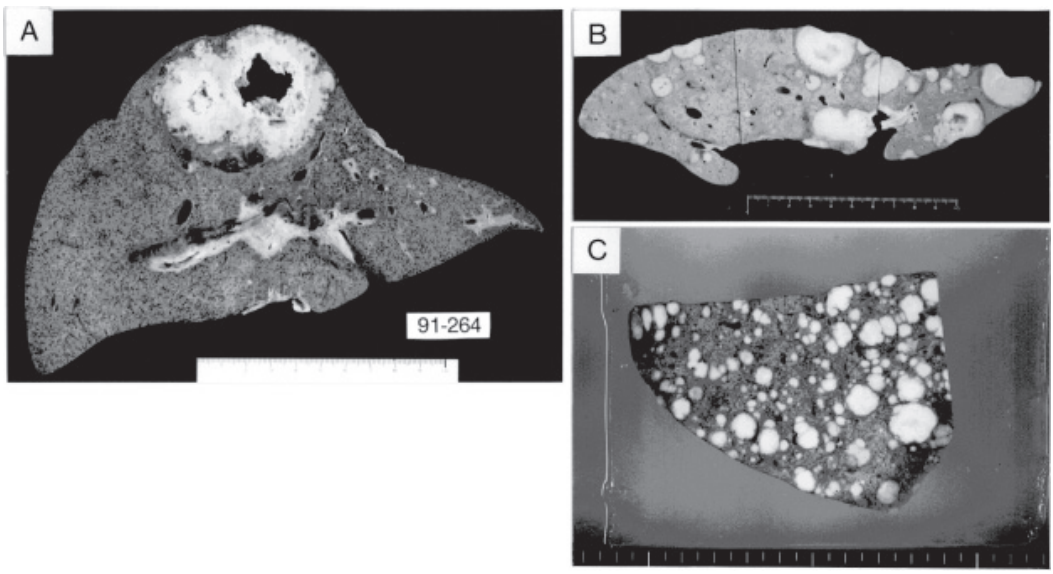

Fig. 2-11. Livers from three autopsy cases dying from carcinoma of the pancreas or large intestine. Metastatic nodules are dispersed in the livers but the size and dimension of nodules are various. Reproduced from Yamanami, Takahashi *et al.* (1999): Anal Quant Cytol Histol 21, pp. 220.

pathological studies. Yet, aside from a few attempts performed so far (Cameron *et al.,* 1988; Tabuchi *et al.,* 1991), we are still far from obtaining systematic knowledge about the quantitative-morphological aspect of hepatic metastasis. If one attempts to enumerate all the metastatic nodules contained in a liver, it will take him or her a great deal of time.

The metastases in this problem are hematogenous ones, presenting as nodular colonies of cancinoma cells delivered from the primary site to the liver via the portal blood flow. Usually they present as spherical nodules of varying dimension, dispersed in the liver uniformly but with varying density, as shown in Fig. 2-11. In the lower right (C), numerous small nodules are densely dispersed, whereas in the upper left (A), there seems to be only a large nodule having a central cavity. The upper right liver (B) presents an intermediate pattern. In geometric terms, the metastatic nodules appear more perfectly spherical than the pancreatic islets, making it seem much easier to apply the model of dispersed spheres. However, there is a problem: the dimension of nodules greatly varies, ranging from a fist-sized mass to clumps of small number of carcinoma cells not identifiable without using microscope.

Circle diameter measurement (Fig. 2-12)

Recently an attempt was undertaken by Yamanami *et al*. (1999). This time, the study was designed to measure, instead of chord length, the diameter δ of circular sections emerging in microscopic slides or macroscopic organ sections (Fig. 2-12). Gross nodules that were already identifiable with the naked eye were measured directly on liver slices, and small ones were subjected to micromorphometry.

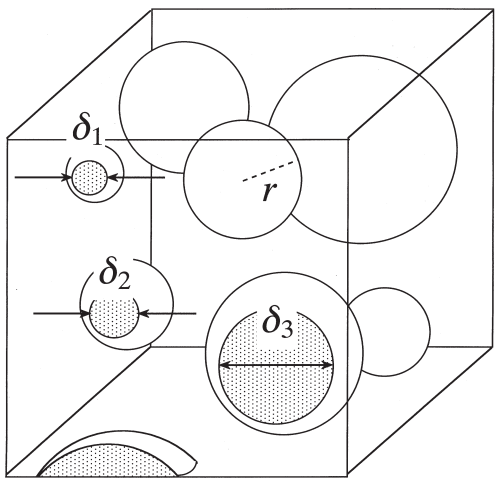

Fig. 2-12. Masurement of circle diameter δ of metastatic nodules on liver section. Reproduced from Yamanami, Takahashi *et al.* (1999): Anal Quant Cytol Histol 21, pp. 218.

Logarithmic normal distribution assumed for sphere radius (Figs. 2-13, 2-14)

Here again, the radius r of spherical nodules was assumed to follow a distribution function, but in this study, logarithmic normal distribution was employed:

$$p(r) = \frac{1}{\sqrt{2\pi}mr} \cdot \exp\left[\frac{-\left(\ln r - \ln r_0\right)^2}{2m^2}\right]. \tag{2-5}$$

Figure 2-13 shows an example of logarithmic normal distribution having a skew pattern, with a peak positioned in a small range of r. The figure expresses the distribution in the form of $p(r)$, the probability function of r, which means

$$p(r) = N(r) / N_V.$$

For the detailed mathematical derivations, see the original article.

The assumption of logarithmic normal distribution for the radii of metastatic nodules was not based on a strict biological background but mainly on account of its mathematical relevance. As in Fig. 2-14, the conformity of this assumption was confirmed in a liver harboring a number of metastatic nodules by comparing the theoretically induced curve of $p(r)$ with the result of actual measurement of nodular radii.

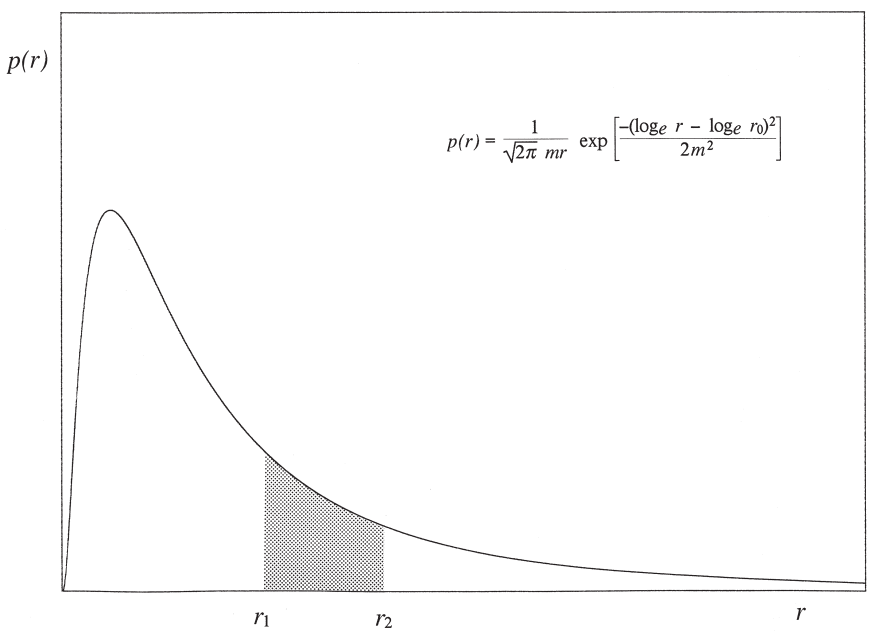

Fig. 2-13. Logarithmic normal distribution. The pattern of distribution resembles Weibull and gamma distributions.

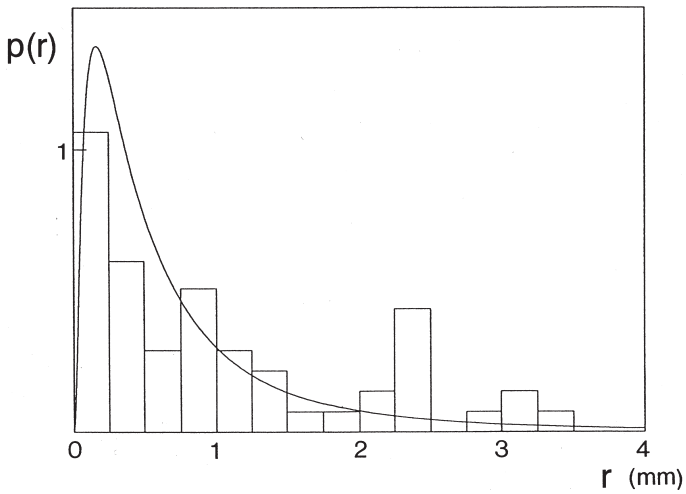

Fig. 2-14. The radial histogram of metastatic nodules directly determined on serial sections of an autopsy liver, shown together with the curve of $p(r)$ theoretically induced. Sufficient agreement of $p(r)$ with the histogram justifies to assume logarithmic normal distribution for $p(r)$. Reproduced from Yamanami, Takahashi *et al.* (1999): Anal Quant Cytol Histol 21, pp. 222.

Here, in sampling the nodules, we relied upon the disector method, a design-based technique of granulometry introduced by Gundersen *et al*. (1984). One can see the theoretical curve sufficiently approximating the result of measurement, justifying to assume logarithmic normal distribution for $p(r)$.

Measurement data of hepatic metastases (Table 2-1)

The basic material of this study was autopsy livers from a total of 31 patients, in all of whom the liver had metastases of carcinoma. Apart from a patient in whom the tumor originated from the lung, in all the cases the primary carcinoma arose in organs drained by the portal system: the stomach, large intestine and pancreas. Listed in Table 2-1 is the result of estimation. The most remarkable finding in this table is that there is a great variance in N, the total number of metastatic nodules contained in the liver. Even in Case 1 in which the total number was estimated to be the minimum of the 31 cases, N was shown to be as large as 10. For surgical oncologists who are pushing forward aggressive treatments for hepatic metastasis, this may be a disappointing result. However, it should be kept in mind that what we obtained was from autopsies. The result would not be the same if investigation were made on patients who were alive and, from a general status point of view, eligible for partial hepatectomy. The largest estimate of N is found in Case 31 of pulmonary carcinoma where the number was shown exceeding 300,000. Between these extremes, there are a series of different estimates ranging almost continuously.

Table 2-1. The cases examined and the results of morphometry for the metastatic nodules in the liver. N_V: the number of nodules in a unit volume (/cm^3). N: the estimate for the total number of nodules contained in the liver. Reproduced from Yamanami, Takahashi *et al.* (1999): Anal Quant Cytol Histol 21: pp. 220.

Case No.	Primary site	mean r (mm)	N_V (/cm^3)	Liver weight (g)	N
1	Colon	12.39	0.01	1,450	10
2	Stomach	9.54	0.02	780	13
3	Pancreas	4.56	0.08	980	80
4	Pancreas	5.51	0.08	1,600	136
5	Rectum	4.36	0.03	4,110	139
6	Pancreas	5.22	0.08	1,980	154
7	Pancreas	0.76	0.41	960	389
8	Stomach	2.12	0.19	2,500	470
9	Stomach	0.50	0.66	830	549
10	Stomach	2.36	0.51	1,600	820
11	Pancreas	2.24	0.26	3,230	834
12	Pancreas	1.91	1.22	1,120	1,369
13	Colon	1.61	1.08	1,390	1,502
14	Pancreas	0.73	2.38	1,230	2,921
15	Pancreas	0.62	4.72	760	3,586
16	Pancreas	0.84	2.26	1,900	4,285
17	Gallbladder	0.57	4.13	1,300	5,364
18	Pancreas	0.85	5.25	1,300	6,826
19	Pancreas	0.56	6.18	1,130	6,986
20	Stomach	0.55	3.48	2,160	7,512
21	Stomach	0.83	6.70	1,150	7,708
22	Biliary tract	0.83	8.24	1,300	10,713
23	Colon	0.62	4.16	4,450	18,494
24	Pancreas	0.52	13.9	1,690	23,423
25	Pancreas	0.52	16.3	1,950	31,824
26	Pancreas	0.51	18.1	2,042	37,006
27	Pancreas	0.21	32.0	1,220	39,089
28	Colon	0.32	36.5	3,490	127,490
29	Stomach	0.21	91.6	1,400	128,170
30	Stomach	0.49	61.8	2,810	173,546
31	Lung	0.36	156.0	2,100	326,970

Correlation between *N* and mean radius (Fig. 2-15)

In Fig. 2-15, the total number N of metastases in the liver is correlated with the mean radius of nodules. A negative correlation is apparent, showing that the larger the mean radius of nodules, the smaller their total number. This correlation seems worthy of special attention. It demonstrates that when in a patient, a metastatic nodule of

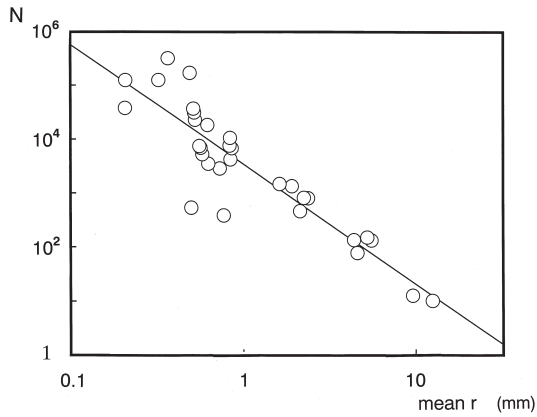

Fig. 2-15. The total number *N* of metastatic nodules in a liver is correlated with the mean nodular radius, plotted on bilogarithmic coordinates. Note quite a significant negative correlation. Reproduced from Yamanami, Takahashi *et al.* (1999): Anal Quant Cytol Histol 21, pp. 221.

extraordinary dimension was visualized in the liver, there is little need to worry about the possibility that in their surroundings, smaller nodules may abound and escape detection at computerized tomography (CT) or other clinical imaging. This will be a good news for those looking forward to seeing a successful treatment for metastatic liver tumors.

d) Alveolar surface area of normal and emphysematous lungs

Normal and emphysematous lungs (Figs. 2-16, 2-17, 2-18, 2-19)

Shown in Fig. 2-16 is a section of normal lung and in Fig. 2-17, that of another lung with advanced emphysema. In the former, the section looks finely spongy, reflecting its structure consisting of a huge number of alveolar air spaces that are separated by thin membranous septa. Instead, in the latter, the lung consists of cavernous spaces of varying size, while normal spongy tissue is left among the spaces only as rudimentary remains.

The difference in the structure between the normal and emphysematous lungs is more clearly visible in their microscopic pictures. As in Fig. 2-18, the normal lung consists of a large number of alveoli, minute air spaces of about 200 μm in diameter, each opening into an alveolar duct. A pair of neighboring alveoli are separated with an interalveolar septum that is about 12 μm thick and contains a dense network of capillaries. Figure 2-19 is from an emphysematous lung. Although the figure presents an early stage of emphysematous changes, the alveolar clusters found in the normal lung are lost and replaced by irregular air spaces that are much larger than the ordinary alveoli. The development of emphysema from a normal lung can be attributed to destruction of alveolar septa due to various noxious agents, particularly long-term smoking. After having been exposed to such agents, the alveolar septa are injured, torn and destroyed, giving rise to the creation of cavity-like common spaces.

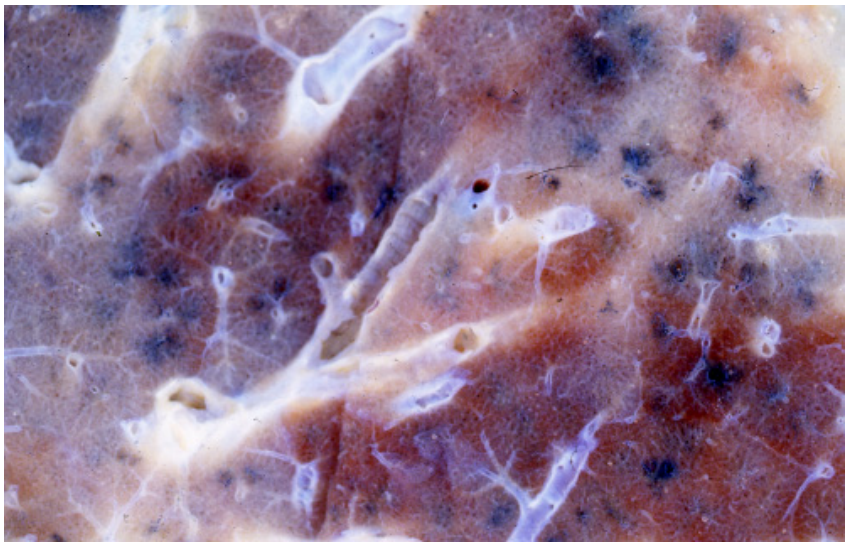

Fig. 2-16. A close-up sectional appearance of normal human lung. The alveolar tissue looks like a sponge, where the individual alveoli are beyond confirmation by naked eyes.

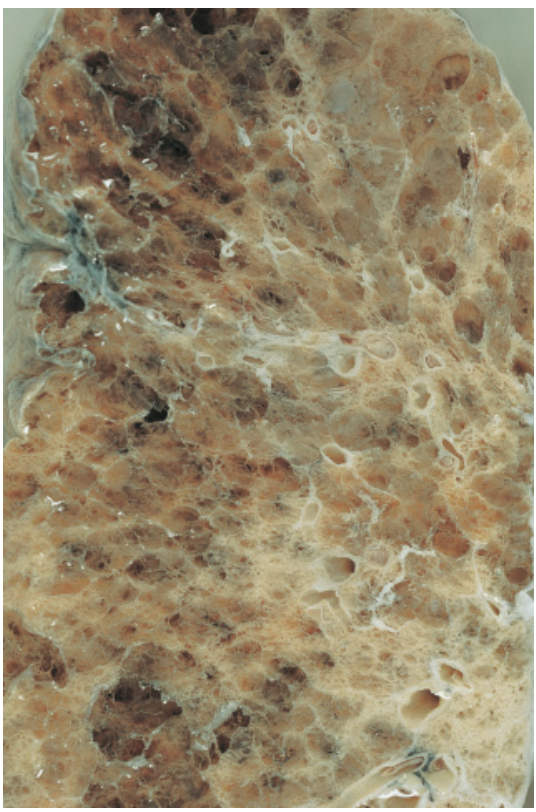

Fig. 2-17. A close-up sectional appearance of lung with advanced emphysema from a patient dying of respiratory failure. Compare with the normal lung of Fig. 2-16. The lung contains grossly cavernous spaces, with the finely spongy alveolar tissue of the normal lung remaining only rudimentarily between the cavities.

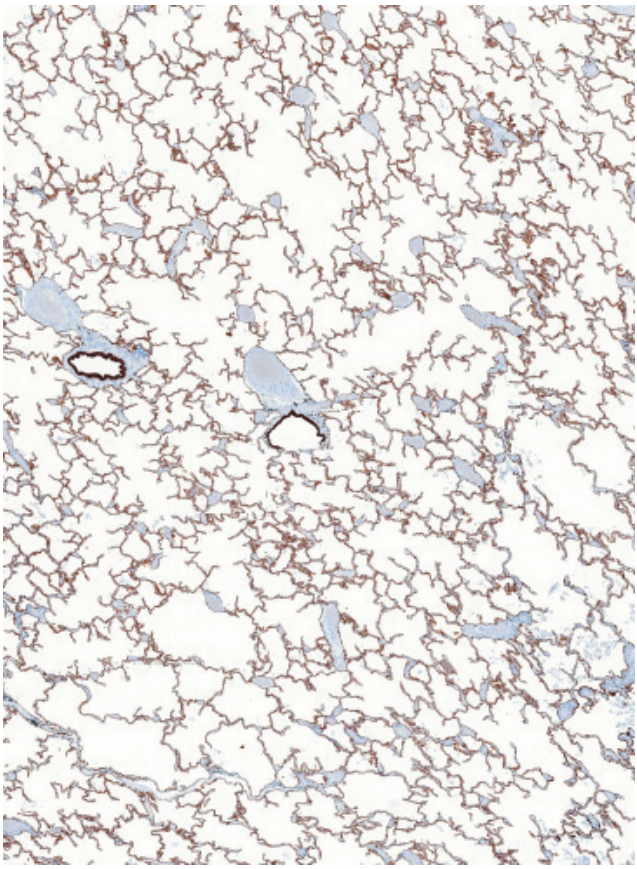

Fig. 2-18. A low power microphotograph of normal lung. The tissue comprises a vast number of alveoli, each about 0.2 mm in diameter. Immunostain for cytokeratin (pan).

A patient having emphysema more or less suffers from respiratory distress, and this primarily is due to the loss of significant part of alveolar septa contained in the lung. Since the septa contain a fine meshwork of elastic fibers, the advancement of emphysematous changes implies that the elasticity retained by the normal lung has been reduced, making it difficult for the lung to shrink during expiration. It also happens that in such lungs, airways more or less have difficulties in keeping themselves open during expiration. This is because of the reduced density and loss of alveolar septa. While in a normal lung, several septa are attached to the wall of an airway, pulling it outward with "recoil pressure," in emphysema the decrease or loss of recoil makes an airway quite vulnerable to collapse and obstruction during expiration, when the pressure around the airway can exceed the internal pressure. On the other hand, the surface of the septa is the place where gas exchange takes place between the alveolar air and the blood flowing through the capillaries running in the septa. Thus, from a structure-function correlation point of view, it seems quite significant to estimate the

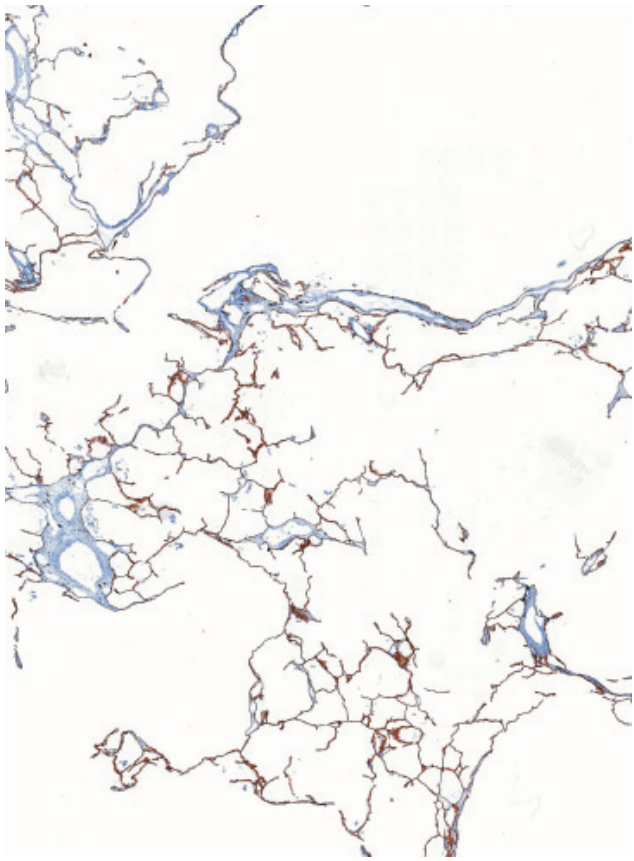

Fig. 2-19. A low power microphotograph of lung in an early stage of emphysema. Note the markedly reduced density of alveolar septa. Immunostain for cytokeratin (pan).

total surface area of septa in the normal lung and its changes in emphysema.

Line sampling of alveolar septa (Fig. 2-20)

Figure 2-20 is a schema showing the stereological method to estimate the total surface area of membranous structure like the alveolar septa. The figure presents a microscopic picture of alveolar tissue, and here we suppose that a sampling line (S.L.) was randomly drawn. The line will come to intersect many alveolar septa, but here we define the intersection as the crossing of the line with the basement membrane of alveolar epithelia (confirm that there are eight intersections). This is because a patch of alveolar septum has two sides, each serving as a surface through which diffusion of gas takes place. Therefore, when the line comes to penetrate a septum, two intersections usually occur. Now, we assume that as a result of measurement, N intersections were generated along a line of sufficient length L. Then, we can calculate $N_L = N/L$, which gives the number of intersections arising over a unit length of the line; in terms

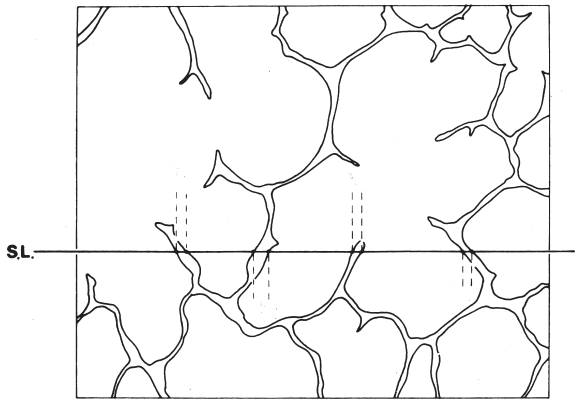

Fig. 2-20. A schema illustrating the line sampling of alveolar septa to estimate the surface area density (S_V). A sampling line (S.L.) is randomly overlaid on a microscopic section of lung, and the number of intersections of the line with epithelial basement membrane is counted. In the figure, eight intersections are confirmable. The number of intersections per a unit length of line (N_L: the numerical density along a line) is calculated, and S_V is estimated by $S_V = 2\,N_L$. Reprodued from Takahashi *et al*. (1994): Human Pathol 25, pp. 704.

of stereology, N_L is expressed as the numerical density of points along a line. Now, if the surface area of septa in a unit volume of lung tissue is S_V, we can obtain its estimate by the equation

$$S_V = 2\,N_L\,. \tag{2-6}$$

This is one of the basic principles of stereology, and S_V is called the surface area density. Its mathematical derivation can be shown in various ways but one may be recommended to refer to the explanation given by Hennig (1956) or Weibel (1962, 1963). There is a restriction placed on the application of this formula. It can work only when the membranous structures one is going to measure are distributed sufficiently randomly in the space with regard to their orientation, a requirement that appears to be well satisfied for the alveolar septa of lung.

Note that S_V obtained as above is the surface area density and not the total area contained in the lungs. The total area S_{total} contained in the lungs is given by multiplying S_V by the volume of both lungs combined.

S_V of alveolar septa: normal and emphysema (Fig. 2-21)

Figure 2-21 exhibits S_V estimated by Suwa and associates in 1966 in lungs from 50 autopsy cases (the present author was not collaborating). The figure includes data from 35 non-emphysematous subjects, where one can see that apparently, S_V decreases with age. The fall of S_V during the postnatal growth may be understood as expressing the enlargement of the lung. However, the value keeps lowering even after the subjects have come of age, falling at 80 years to a level as low as half that of the young adult. In patients having emphysema, S_V is shown to have significantly been reduced

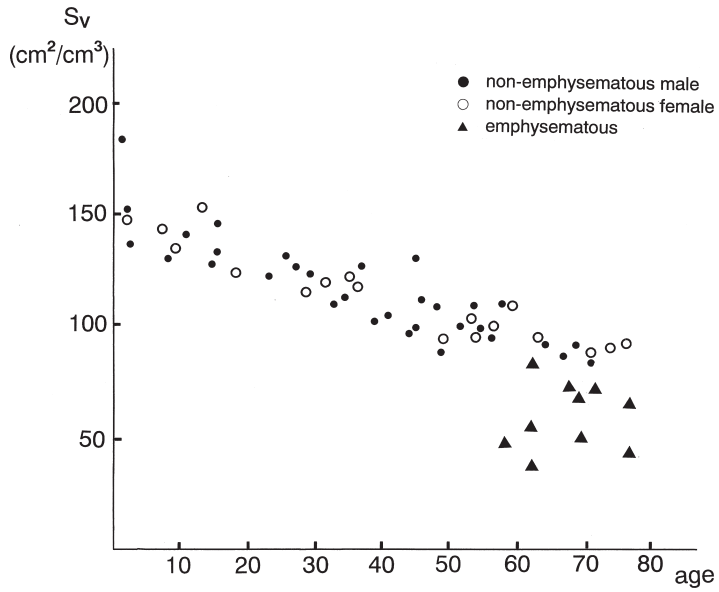

Fig. 2-21. The surface area density S_V of alveolar septa in autopsy lungs from 50 patients, including 15 with emphysema. Note that S_V linearly falls with age even in non-emphysematous subjects. S_V is significantly reduced in emphysematous lungs.

compared with the non-emphysematous subjects. It seems that even in the absence of emphysema, the lung undergoes slow but continuous loss of alveolar septa, coming to be in a slightly emphysematous state in advanced ages.

e) Remodeling of alveolar structure in paraquat lung

Fibrosis in advanced paraquat lung (Figs. 2-22, 2-23)

To be presented next are examples of analysis where a simplified geometric model is introduced to assimilate the microstructure and describe its changes in quantitative terms. The first example deals with fibrosis of lung in patients intoxicated by paraquat, where estimation of S_V is combined with that of V_V. The earliest lesions, produced experimentally by giving paraquat to hamsters were shown above (Figs. 2-1 and 2-2). As described there, patients intoxicated with paraquat suffer from severe respiratory distress that emerges on Day 4 or 5 and deteriorates thereafter.

Figure 2-22 presents the macroscopic picture of lung from a patient of paraquat intoxication who died of respiratory failure, presenting lung fibrosis in the terminal stage. Figure 2-23 is from another case, and here, the spongy tissue of ordinary lung (shown in Figs. 2-16 and 2-18) is replaced with a dense mass of collagen (green), sparsely penetrated by alveolar ducts that remain and are more or less dilated. Usually, the lung lesions reach this stage about one month after ingestion, and by the time the

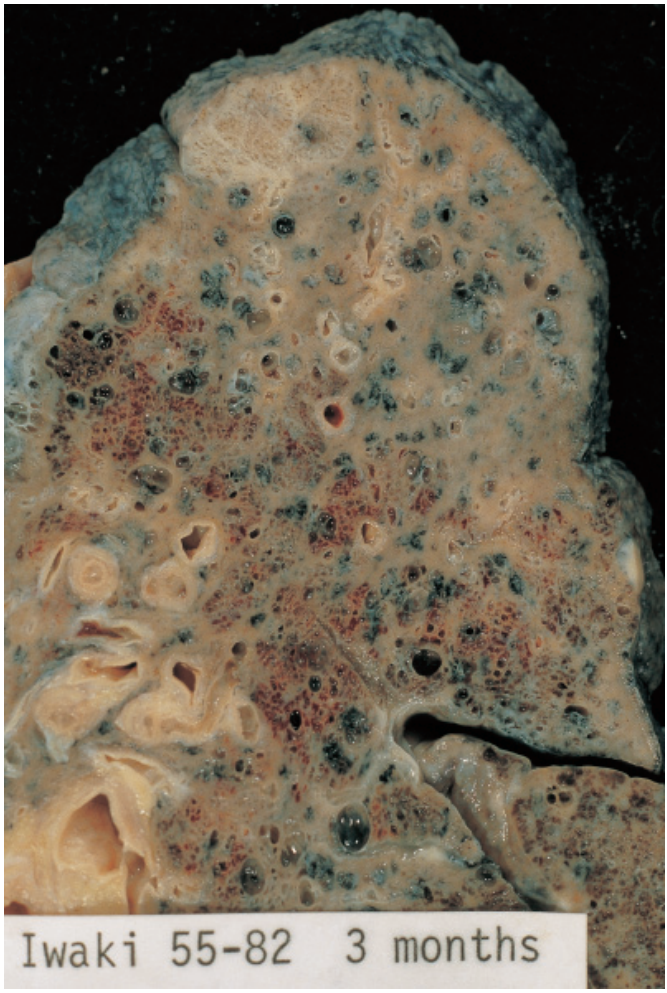

Fig. 2-22. The sectional appearance of lung from a patient of paraquat intoxication dying three months after ingestion. Diffuse induration of the organ resulting from advanced fibrosis.

intoxicated patient usually succumbs to respiratory failure. To study how the changes of lung begin, develop and culminate in this state, morphometric analysis was undertaken of autopsy lungs from 15 patients dying of paraquat intoxication (Takahashi *et al*., 1994; Takahashi, 1994). The period from paraquat ingestion until death was varying, ranging from 12 hours to 40 days. The analysis helps understand how, from a microstructure point of view, paraquat-associated lung injuries begin and advance toward the terminal stage of pulmonary fibrosis, where the alveolar structure has been severely remodeled.

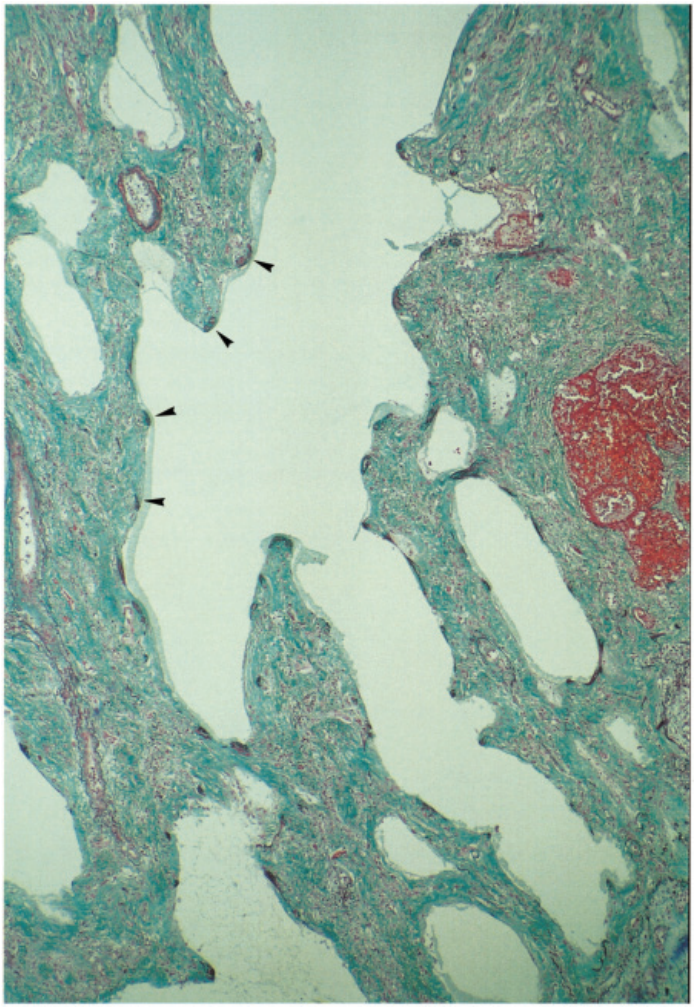

Fig. 2-23. Microscopic appearance of paraquat lung in an advanced stage. The normally spongy lung tissue (see Fig. 2-18) is replaced by dense masses of collagen (green). There are remains of branching air spaces that correspond to alveolar ducts. Visible along the spaces are black dots, and these are the entrance rings of alveoli (arrowheads). Elastica-Goldner stain.

Deposition of matrix layer on alveolar septa in early paraquat lung (Figs. 2-24, 2-25)

Shown in Figs. 2-24 and 2-25 is the lung of a patient dying on Day 13 of intoxication. In Fig. 2-24, although one can find alveoli still retaining their septa (blue), there are mesenchymal cells vigorously proliferating on the septal surface and beginning to produce collagen in the surroundings. Attention is to be paid to the finding that there is a jelly matrix layer, stained faintly in violet and possibly containing proteoglycans, extending on the surface of the septa.

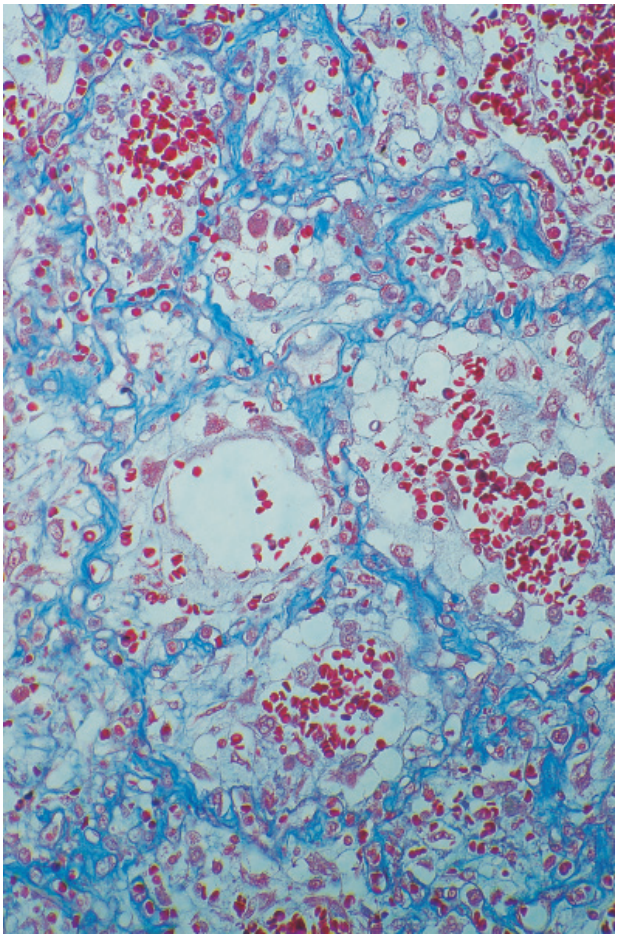

Fig. 2-24. Microscopic appearance of lung from a patient of paraquat intoxication dying on the 13th day. There are several alveoli in the picture, all containing matrix substance (stained homogeneously faint blue) in which mesenchymal cells are proliferating. Azan-Mallory stain.

In Fig. 2-25, where the contours of matrix layer are illustrated in a collateral sketch, it seems that the layer is deposited on the surface of alveolar septa at a certain thickness, narrowing the air spaces correspondingly. It is in this matrix that the mesenchymal cells are proliferating and beginning to secrete collagen. From a lung function viewpoint it may be conceivable that the matrix layer, interposed between the intra-alveolar air and the blood flowing in the capillaries embedded in the septa, acts as a barrier to diffusion of O_2 as well as CO_2. Also the matrix, mucous in itself and diffusely stuck to the alveolar surface, may significantly impair the ventilation function of lung by restricting the elasticity of normally thin, membranous septa. Thus the septa, if the overlying matrix layer is included, are likely to increasingly thicken with the advancement of lung disease, and this mainly accounts for the progressive impedi

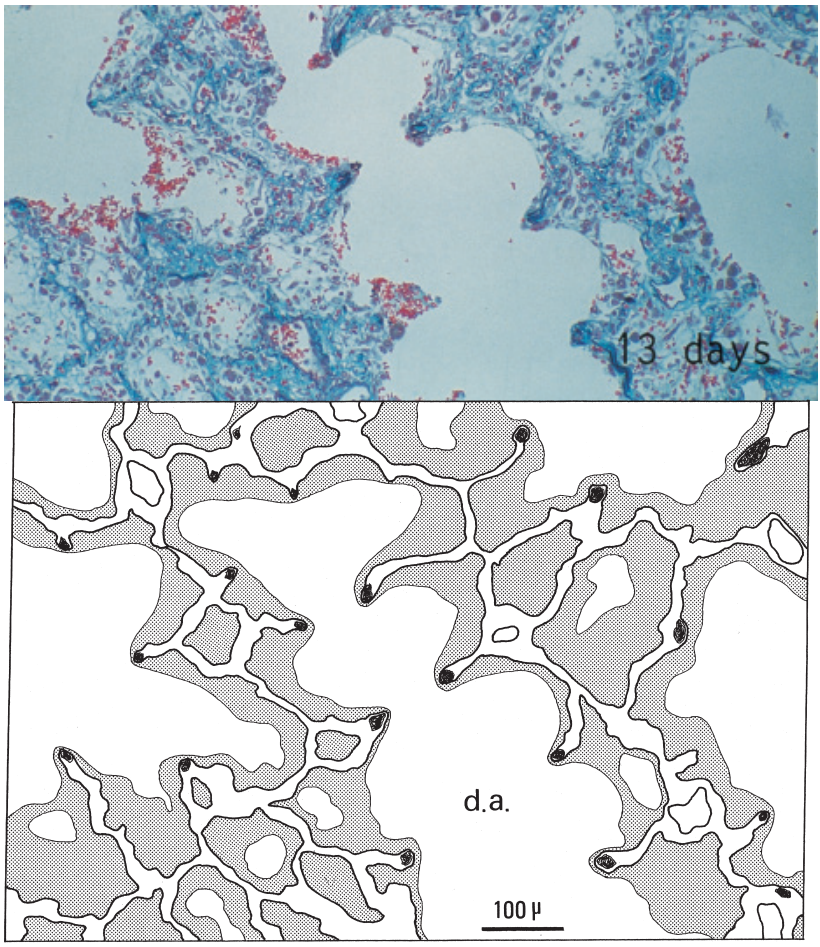

Fig. 2-25. The alveolar septa, the matrix layer deposited upon the septa and the remaining air spaces in the above lung, as illustrated below. Reproduced from Takahashi *et al*. (1994): Human Pathol 25, pp. 703.

ment of lung function. Finally, the lung reaches the state of Fig. 2-23, where all the alveolar air spaces have been lost and replaced with mass of collagen deposited in the gelatinous matrix. Thus, the mean thickness of septa including the matrix, if quantified, is considered to serve as an index for the advancement of paraquat-induced lung disease. Here, the problem is how to define the mean thickness of septa, which apparently is a 3-D quantity.

The plate model for the determination of septal thickness (Fig. 2-26)

Figure 2-26 schematizes a geometric model which was introduced to define the thickness of membranes or plates randomly dispersed in the space. Suppose, as in the figure, a cubic lung tissue contains a sufficiently large number of alveoli. For the sake

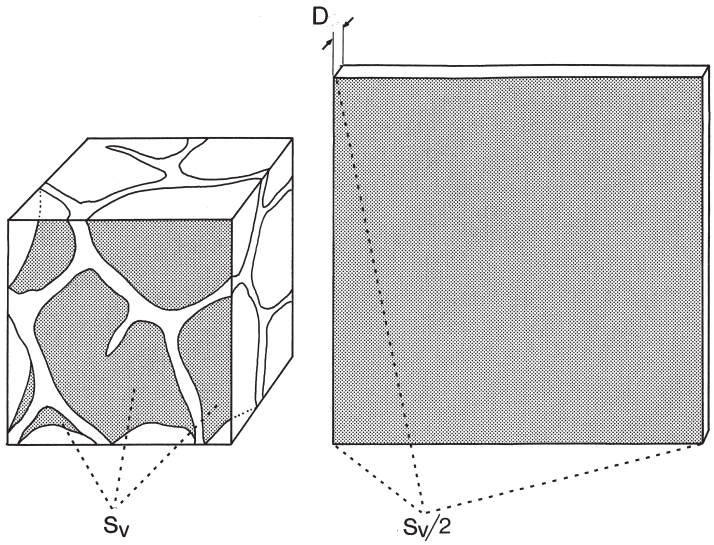

Fig. 2-26. The plate model for the determination of mean septal thickness. Suppose that we estimate stereologically, in a unit volume of cubic lung tissue, the volume V_V and the surface area S_V of alveolar septa contained. Next suppose that we transform the septa into a plate of uniform thickness, with V_V in volume and S_V in surface area. Then the thickness D of this plate gives the mean thickenss of septa. Reproduced from Takahashi *et al*. (1994): Human Pathol 25, pp. 704.

of simplicity, we assume that the edges of the cube are of unit length. Then we perform measurement on one of its 2-D sections, in this figure on the frontal one. We make on this section line sampling and obtain S_V, the alveolar surface area contained in a unit volume. At the same time, "chord length measurement" of septa is performed, and we obtain V_V, the volume of alveolar septa in a unit volume. Now suppose that we transform the entire septa contained in the cube into a plate of uniform thickness as in the right half of the figure. Consider that this plate is made so as to be of uniform thickness D, with its volume equal to V_V and with its surface area, with the two faces put together, equal to S_V, namely,

$$D\, S_V/2 = V_V.$$

Then we find in the thickness D a quantity that exactly corresponds to the mean thickness of septa in a 3-dimensional sense. This is a method of analysis we express as the plate model.

Increasing thickness of septa after paraquat ingestion (Fig. 2-27)

The result of morphometry is shown in Fig. 2-27. Here D, the mean thickness of septa, is plotted in the ordinate, and the days after paraquat ingestion in the abscissa. In the early stage of intoxication D remains about 12 μm, a value not significantly different from the alveolar thickness in normal lungs. One can see that D begins to rise on about the 7th day. It accelerates to thicken thereafter, following a course which is

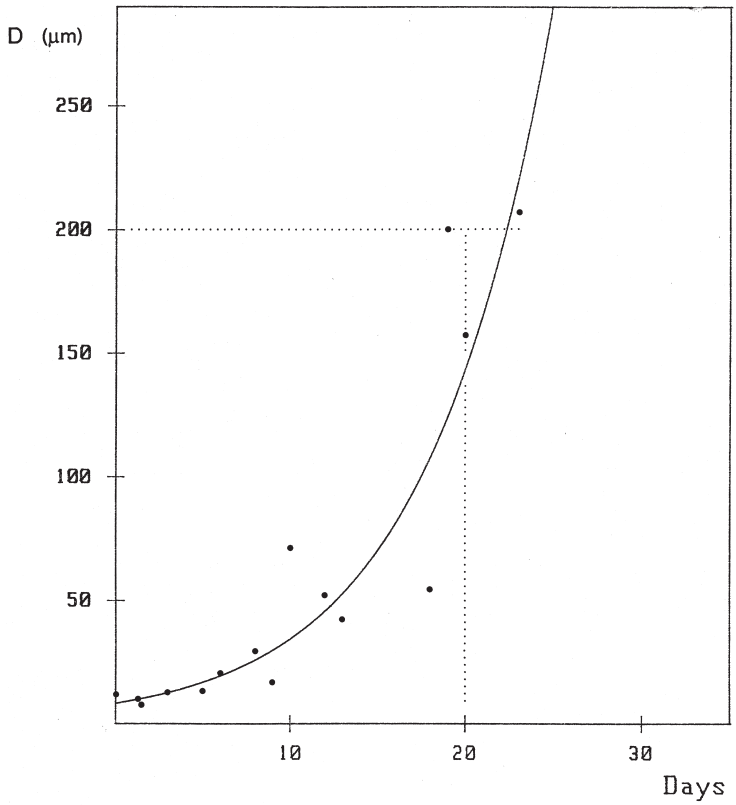

Fig. 2-27. *D*, the mean thickness of alveolar septa, is presented against the days after paraquat ingestion. The elevation of *D* with days is assimilated with an exponential function. *D* reaches 0.2 mm about three weeks after ingestion, showing that by this time, the alveoli have totally been obliterated. Reproduced from Takahashi *et al*. (1994): Human Pathol 25, pp. 705.

approximately exponential, as shown by the curve. Note that *D* attains a level of 200 μm twenty days after taking paraquat.

Weibel (1963), in his extensive morphometric studies of lung, estimated the mean depth of a single alveolus at about 200 *μm*; he gave about the same estimate for the mean diameter of its opening to the alveolar duct. According to this, one may interprete the above result as suggesting that by about 3 weeks after ingestion of paraquat, the septa have become so thick as to completely obstruct the alveolar air spaces. That this really is the case is demonstrated in the lung changes in Fig. 2-23. The lung, from a subject dying on Day 23, presents the alveolar tissue in a state of advanced remodeling. What is found here is severe fibrosis of lung; the alveolar tissue has changed into a mass of dense collagen (stained in green) penetrated by branching duct-like spaces. That these spaces are remains of alveolar ducts is witnessed by the black dots delimiting the spaces: the entrance rings of alveoli (pointed by arrowheads). The rings are mass of elastic fibers encircling the opening of alveoli to the alveolar ducts, reinforc-

ing the alveolar structure. Tracing the rings in the picture, it may be understood that indeed by about 3 weeks of intoxication, the remodeling has finished, with the alveolar air spaces completely obliterated with collagen.

It may be pertinent to give a brief comment on the exponential character of disease advancement shown by the rising *D*. It reflects that with time, the lung disease progresses in a divergent fashion. This may be interpreted as meaning that we are dealing with a phenomenon, in which remission cannot be expected to occur, since there is no room for the curve to reach a plateau, or a state of equilibrium. This may be an essential difference from a phenomenon in which adaptation can be expected to take place, an example of which has been presented in the medial hypertrophy of arteries in hypertensive subjects.

f) Changes of bone trabeculae in oeteoporosis — a cylindrical model

Spongy bone: normal and with osteoporosis (Figs. 2-28, 2-29)

Osteoporosis is a disease debilitating many senile persons who are liable to fracture due to age-related fragility of bones. Figure 2-28 demonstrates a microscopic

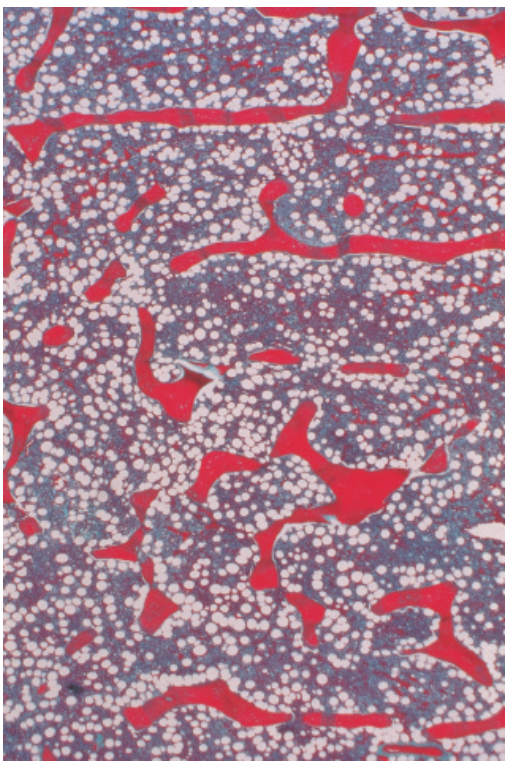

Fig. 2-28. Low power microphotograph of normal spongy bone taken from the body of lumbar vertebra. Bone trabeculae, the beam of framework, are shown retaining a certain thickness and arranged at a certain density. Extending around the trabeculae is bone marrow. Elastica-Goldner stain.

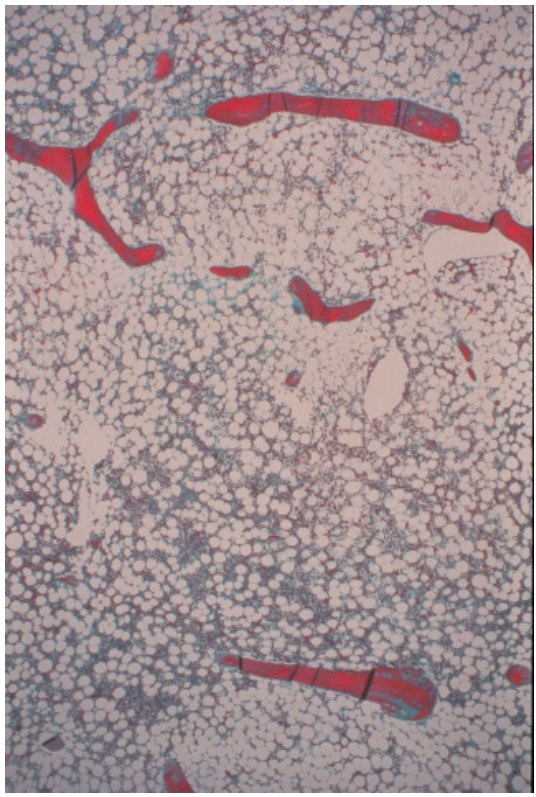

Fig. 2-29. Low power microphotograph of vertebral body with osteoporosis. Note that the density of trabeculae as well as their thickness appear significantly lower than the normal bone shown in Fig. 2-28.

picture of normal spongy bone, the body of lumbar vertebra taken from a young adult male, and Fig. 2-29 that from an aged female with osteoporosis. While the non-osteoporotic bone contains sturdy bony trabeculae forming a dense 3-D network, the trabeculae in the bone of the aged seem thinner and sparsely arranged. On this difference, it seems quite understandable that in the latter, fracture occurs frequently and at a slight mechanical load. However, ambiguities still remain about the morphogenesis along which the structural bone changes advance toward the state of severe osteoporosis. Is osteoporosis simply reflecting a symmetric thinning of trabeculae, or, do some topological changes occur in the trabecular network itself? At least in some aspects, this is a problem which may require studies by 3-D morphometry. The following is a summary of recent attempt made by Sugawara *et al*. (2003).

Trabecular bone mass: changes with aging (Fig. 2-30)

The volume density V_V of bony trabeculae was estimated by point counting on silver-impregnated sections of spongy bone. The material was the bodies of lumbar vertebrae (L3 or L4) taken from a series of 56 autopsy patients, with the age ranging

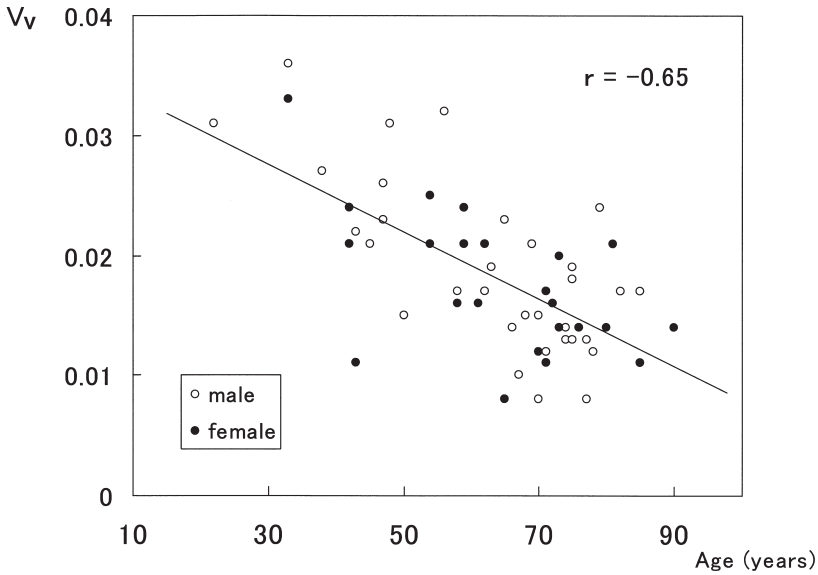

Fig. 2-30. V_V, the volume density of trabeculae estimated by point counting on microscopic sections of lumbar vertebral bodies from 55 autopsy cases. Apparently the density tends to fall with aging.

from 21 to 90 years. As shown in Fig. 2-30, the volume density of trabeculae decreases with age, clearly demonstrating the progress of osteoporosis. There are studies reporting data like this (Beck *et al*., 1960; Hedlung *et al*., 1988), but a problem still remains: whether symmetric thinning of individual trabeculae, or loss of trabecular segments, or both, is responsible for this age-dependent reduction of bone mass?

The cylindrical model for the determination of trabecular radius and length (Fig. 2-31)

In order to obtain estimates on the mean thickness and the length of trabeculae in a unit volume, we introduced a geometric model, in which the structure of spongy bone was assimilated to a network made of cylindrical trabeculae, as in the schema of Fig. 2-31. S_V, the surface area of trabeculae in a unit volume, is easily obtained by the microscopic line sampling. V_V, measured by point counting, is already at hand. Here let us assume that the whole trabeculae in a unit volume of spongy bone were joined to form an elongated trabecula which is cylindrical in shape, L in the total length and with a uniform radius R. We assume that the volume of the cylinder is equal to V_V and its lateral surface area is S_V. In this setting, L corresponds to the total length of trabeculae contained in a unit volume, and therefore is to be renamed as the length density L_V, according to the systematized wording employed in stereology (Weibel, 1979). Then

$$\pi R^2 L_V = V_V \quad \text{and}$$

$$2\pi R L_V = S_V.$$

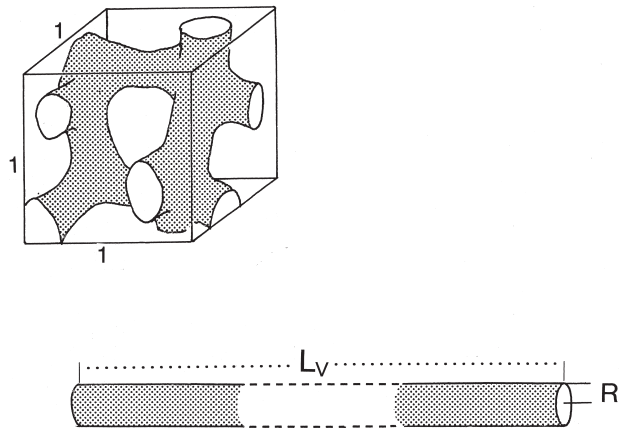

Fig. 2-31. The cylindrical model for geometric treatment of bone trabeculae. Suppose that the trabeculae in a unit volume of spongy bone are transformed into a cylinder of uniform radius R, during which process, V_V and S_V of trabeculae are kept unchanged.

By solving these, we obtain

$$R = 2V_V/S_V \qquad \text{and}$$

$$L_V = S_V^2/4\pi V_V.$$

The changes of trabeular radius and length density with age (Figs. 2-32, 2-33)

Microscopic sections of bone used above in the estimation of V_V by point counting were submitted to line sampling to estimate S_V, and the parameters L_V and R were calculated from V_V and S_V. In Fig. 2-32 the estimates of R, the mean trabecular radius, were plotted against the age of the patients on semilogarithmic coordinates. There seems to be a slight decreasing tendency with the age, but no significant correlation proved to exist. Thus, we were unable to demonstrate an age-related thinning of trabeculae in unambiguous quantitative terms.

On the other hand, L_V, the total length of trabeculae in a unit volume, clearly decreases with age as in Fig. 2-33. On semi-logarithmic coordinates, the correlation coefficient is –0.43 which is significant at $p = 0.01$. With these results of morphometry, the age-related decrease of trabecular mass appears to be associated not so much with thinning of individual trabeculae as with loss of trabecular segments. The process creating this change may be understood as follows. Trabeculae keep bearing an excessive mechanical load, either tension or compression, for a long time. Finally microfracture occurs at some of the trabeculae. The trabeculae disconnected by microfracture, no longer bearing any mechanical load, get atrophied and disappear within a short time. Possibly, trabecular segments are involved in this process one after another, making the whole network of spongy bone increasingly rarefied, creat-

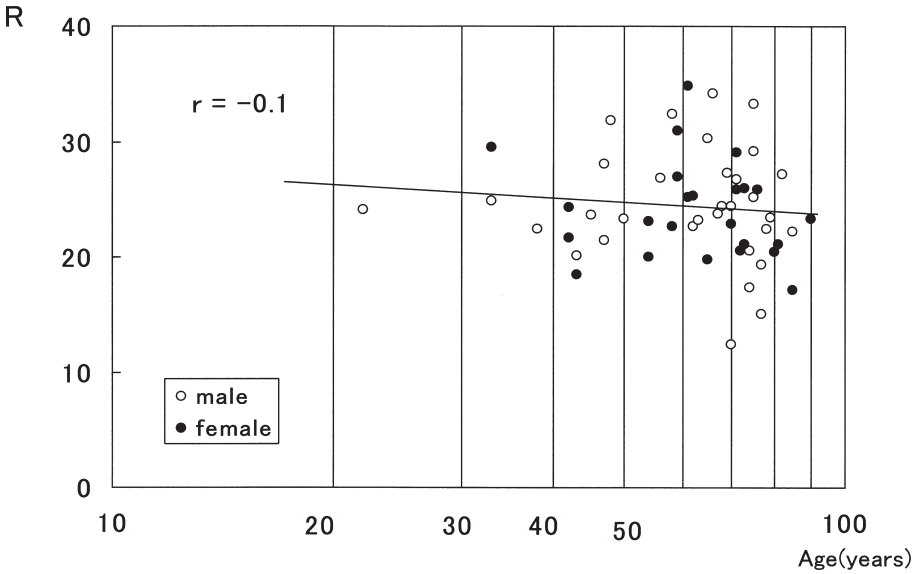

Fig. 2-32. The mean trabecular radius R estimated on 55 patients is shown against the age on hemi-logarithmic coordinates. No significant age-associated changes of R.

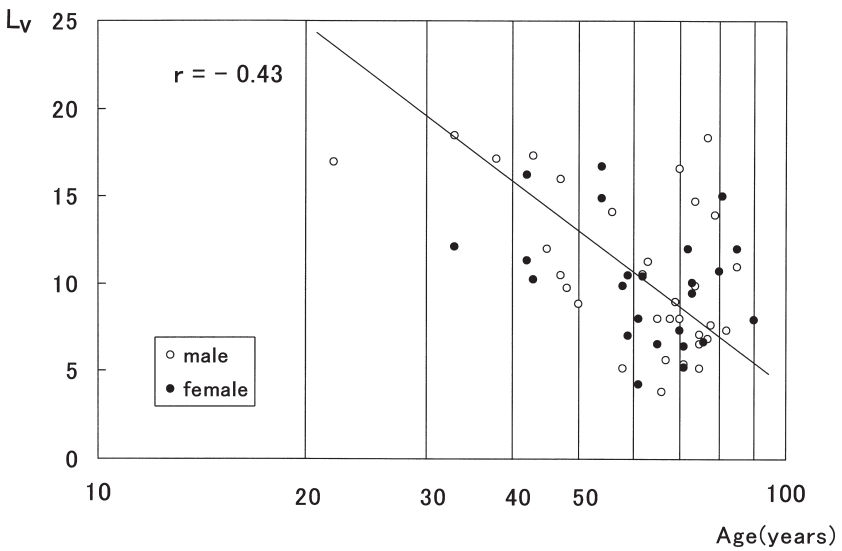

Fig. 2-33. L_V, the length density of trabeculae, against the age. There is a significant negative correlation of L_V with age, showing the progression of age-dependent loss of trabeculae.

ing the state of osteoporosis. Once this process is started, a bone with already rarefied trabeculae gets more susceptible to microfracture, thus putting a vicious cycle in motion.

Three-D structure of spongy bone: normal and with osteoporosis (Figs. 2-34, 2-35)

To examine this possibility, we attempted 3-D visualization of trabeculae. Of the 56 cases studied, vertebral body of a young male aged 21 was selected as a normal control. After being decalcified, the spongy bone was embedded in celloidin-paraffin and was submitted to serial sectioning. From the sectional pictures, the contours of trabeculae were picked up and inputted into a reconstruction-assisting computer system. Figure 2-34 is a 3-D picture of trabeculae reproduced in a display. On the technical aspect of 3-D reconstruction, comments will be given in Chapter 4.

In the figure one can see that in a normal spongy bone, trabeculae are put together into a network, a state which reminds us of the frame of building made of steel beams. Here the individual beams, about equally thick, are shown forming a 3-D network; also the meshes of the network seem to be of about the same dimension and arranged with roughly uniform density.

Figure 2-35 exhibits the changes in 3-D structure of vertebral body in osteoporosis. This is from autopsy of a female aged 71 years. Although at some places the normal network of trabeculae as found in the foregoing picture remains, there are cavernous spaces or fissures, which apparently are produced by loss of trabecular segments. This is a state corresponding to the frame of building where several steel beams

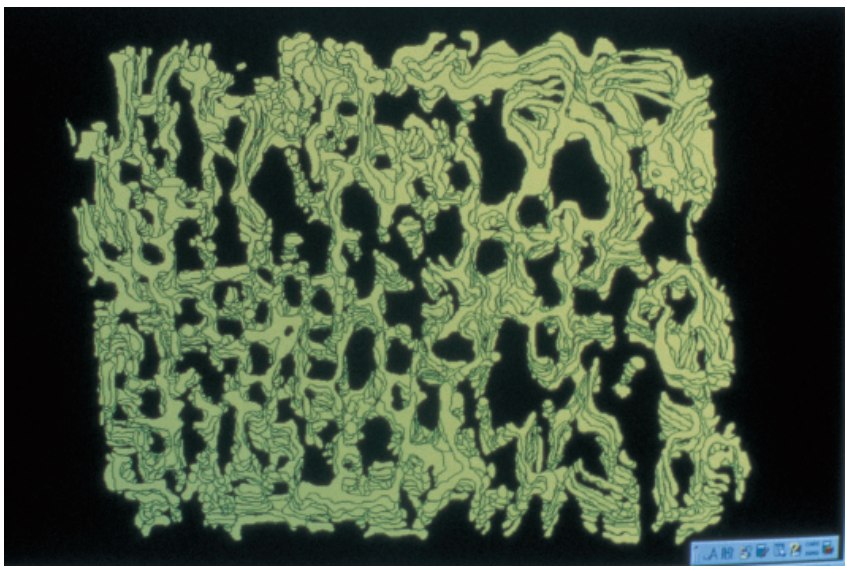

Fig. 2-34. Computer-assisted 3-D reconstruction of non-osteoporotic spongy bone from the body of lumbar vertebra. The trabeculae form a network like the frame of building.

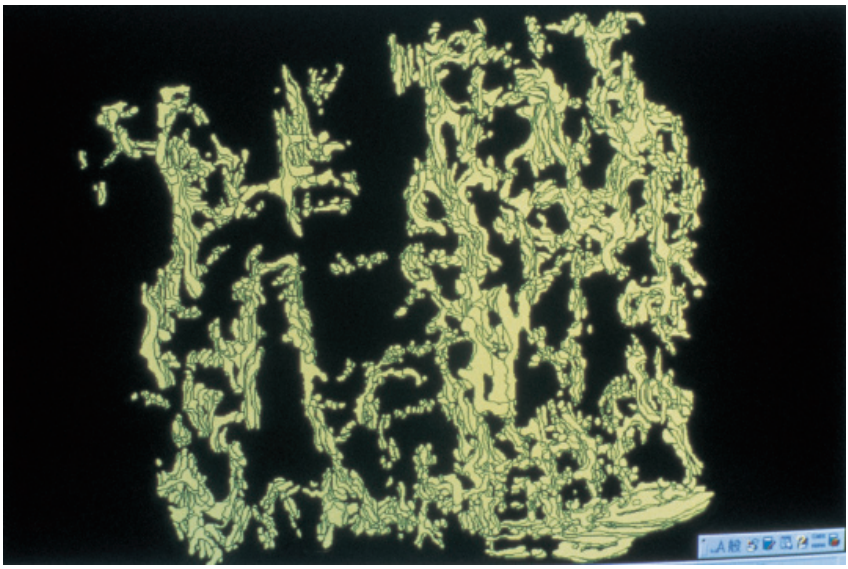

Fig. 2-35. Computer-assisted 3-D reconstruction of osteoporotic spongy bone. Lumbar vertebral body from a female, aged 71 years. Note the rarefied arrangement of trabeculae. There are cavernous spaces left after trabeculae were destroyed.

have been removed from the network. At the fissures, trabeculae seem disconnected by microfracture. It is clear and remarkable that in the spongy bone, fissures tend to extend in the vertical direction. This may be interpreted as suggesting that, of the network beams, mainly the transverse component was torn off by an excessive force pulling the network toward the lateral direction. Possibly, this may be the result of longstanding gravitational burden that continues to press the vertebral body in vertical direction.

Thus osteoporosis of the vertebral body is likely to be a process in which trabecular segments are lost one after another through microfractures, bringing about a typically rarefied, porous bone. Why in some subjects the trabeculae are particularly susceptible to microfracture, and are not in the others, may be accounted for perhaps from the difference in the rigidity and texture of bony trabeculae.

g) The mean radius of hepatic lobules—another cylindrical model

The lobular contour: normal and hepatic-carcinoma-harboring livers (Figs. 2-36, 2-37)

There is a long history of controversies about the way the structural principle of the liver is to be understood. But here let us keep ourselves from being trapped in this debate because we will have to deal with this problem in Chapters 3 and 7. Now let us concentrate on how we can quantitatively measure the growth of liver tissue, either ordinary or pathological, on microscopic level.

For the sake of easier perspective, we assume that the liver is an assembly of the

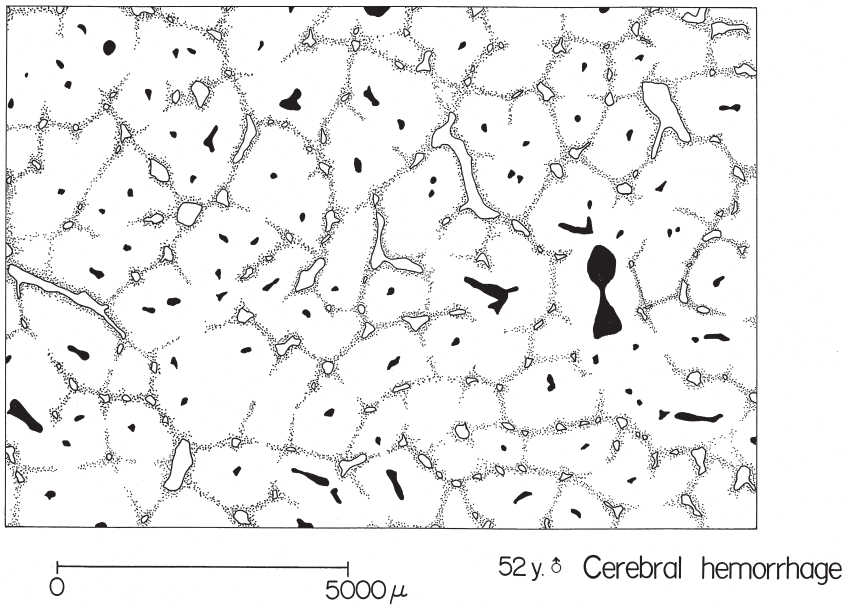

Fig. 2-36. Low power microscopic picture of normal liver of adult, produced by projecting the slide upon a sheet of paper and tracing along the contour of hepatic lobules. Note the approximate size of lobules. Reproduced from Takahashi *et al*. (1968): Tohoku J exp Med 94, pp. 207.

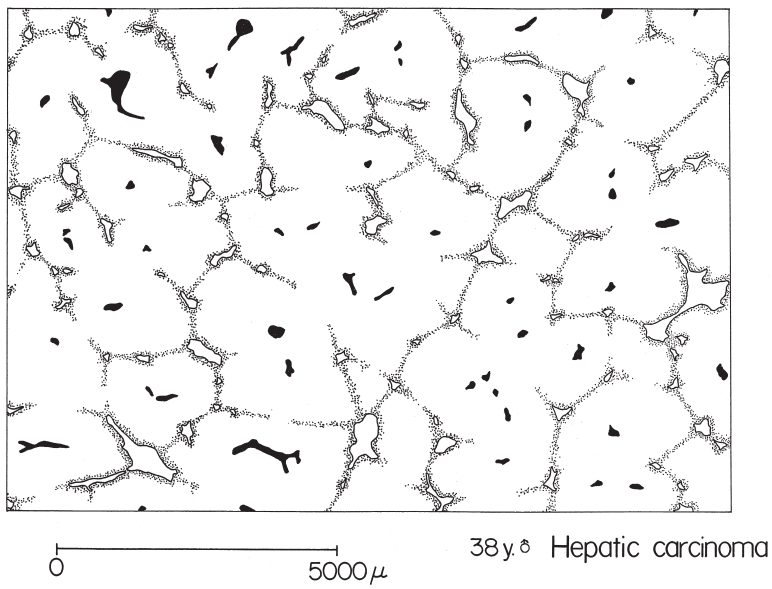

Fig. 2-37. Microscopic picture of a non-cirrhotic liver harboring hepatocellular carcinoma in other parts. The lobular architecture is retained. Compare with the foregoing picture (Fig. 2-36). Apparently the lobules look enlarged to a certain degree. But how can we describe the difference in quantitative terms? Reproduced from Takahashi *et al*. (1968): Tohoku J exp Med 94, pp. 207.

classical hepatic lobules (also variously called like Kiernan lobules, hepatic units or hexagonal lobules). In Fig. 2-36, one can see a sketch of normal liver tissue taken at autopsy. This was drawn by projecting a sheet of microscopic slide of an adult liver at a low magnification. It includes branches of portal (white) and hepatic veins (black), and the borders of hepatic lobules are expressed by shading. In this case, the lobular borders were visible microscopically to a certain degree because of a staining difference among the hepatocytes in the peripheral, intermediate and central zones. Note the approximate dimension of the lobules.

Figure 2-37 is from another autopsy liver, drawn at the same magnification as in the foregoing one. The patient died of hepatocellular carcinoma. However, in the part of the liver spared from tumor, there were no changes suggesting the presence of cirrhosis, chronic hepatitis or other parenchymal hepatic diseases. On account of this, the lobular structure was retained as clearly as the former case, as visualized in the figure.

Compare the two livers. It appears that in the latter liver, the individual lobules are uniformly enlarged. Here one cannot rule out the possibility that the lobular enlargement simply reflects a compensatory hypertrophy, seeing that a significant volume of the organ had been replaced by tumor. But it may also be possible that the enlargement reflects a hepatocellular growth *per se*, which is underlying the development of cancer. In any case, it may be desirable that one can define in quantitative terms whether there is a process of parenchymal growth advancing, and if there really is, to what degree. The growth of the liver as an organ can simply be defined with the increase in its volume, or more practically, in the weight. However, in the present example we have to define the growth not as an organ but on a tissue level. If the parenchymal tissue of the liver is an assembly of unitary structures such as lobules, we will be able to define and measure the parenchymal growth by comparing the size of the units. But it seems an uneasy task if one has to begin with defining the accurate geometric shape of individual lobules before quantification. How can we determine the mean size of lobules, without defining their 3-D shape?

A cylindrical model for the determination of lobular radius (Fig. 2-38)

An attempt was made to define the size of the hepatic lobule with its mean radius R (Takahashi *et al.*, 1968). For this purpose, another cylindrical model was devised. Imagine a sufficiently large cubic liver tissue, with edges of unit length, as in the schema of Fig. 2-38. The cube is of unit volume and contains a sufficient number of hepatic vein branches that are dispersed in the cube. We assume that somehow, we have managed to obtain the total length of hepatic veins contained in this unit cube, or L_V, the length density in space. Next we suppose that the cube is transformed into a cylinder of uniform radius and L_V in length, without changing the volume. Then we see that if the radius of the cylinder is R, it corresponds to the mean breadth of parenchymal tissue surrounding a segment of hepatic vein. Apparently, what is expressed by R corresponds to nothing but the mean lobular radius defined in terms of 3-D geometry, and in this process we have managed to avoid being implicated in the issue of lobular shape.

The length density L_V of hepatic veins can be estimated by resorting to another basic principle of stereology. Suppose that the cubic space is sectioned, as in the figure, with a sheet of plane which is parallel to one of the sides of the cube. The

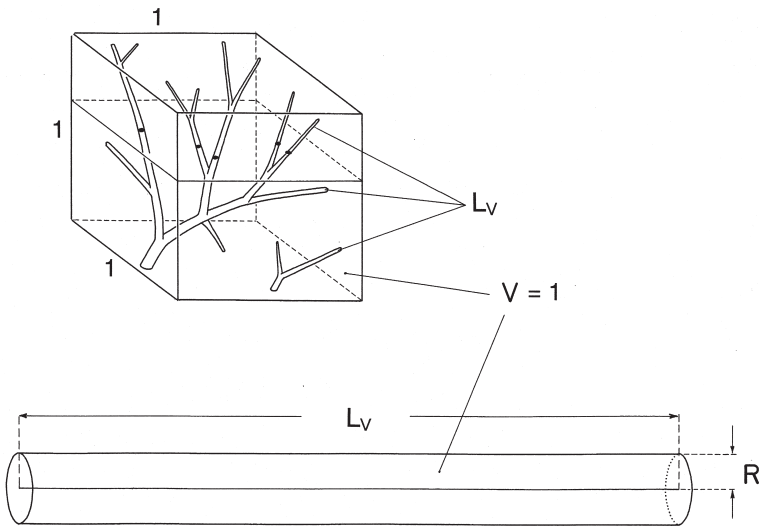

Fig. 2-38. A cylindrical model for the determination of mean radius for the hepatic lobules. The length L_V of hepatic veins in a unit volume of cubic liver tissue (the length density in space) is determined stereologically by $L_V = 2\,N_A$, where N_A is the number of hepatic veins in a unit area of microscopic section (the numerical density in area). Next imagine that the liver tissue is transformed into a cylinder, L_V in length and of uniform radius R, without changing the volume. Then R, corresponding to the mean breadth of parenchyma around a segment of hepatic vein, corresponds to the average lobular radius. Reproduced from Takahashi *et al.* (1968): Tohoku J exp Med 94, pp. 210.

section is a square with edges of unit length, in which a large number of hepatic vein branches emerge as N_A points in the section. N_A denotes the number of points in a unit area, or the numerical density in area. Then, the total length L_V of the branches in the cube is related to the number of their cut points N_A in the section by

$$L_V = 2\,N_A\,. \tag{2-7}$$

For the mathematical derivation of the formula, see the literature (Suwa *et al.*, 1966).

The growth of lobules expressed by *R* (Fig. 2-39)

In Fig. 2-39, the estimates of R from 36 normal livers obtained at autopsy are shown against the patients' age. As defined, R corresponds to the mean radius of lobules, and therefore, the figure expresses how the parenchymal growth of the liver proceeds; in other words, we find here a growth curve defined on a microstructural level. R is about 260 μm in the newborn, rapidly rises until it reaches a plateau at about 18 years of age. It remains thereafter, though scattered, within a range between 350 and 400 μm. The mean R was calculated at 376 μm for the 26 patients older than 18 years. This sufficiently coincides with the lobular radius defined in another way, *i.e.*, as the mean length of the sinusoidal flow routes, which will be shown in the next

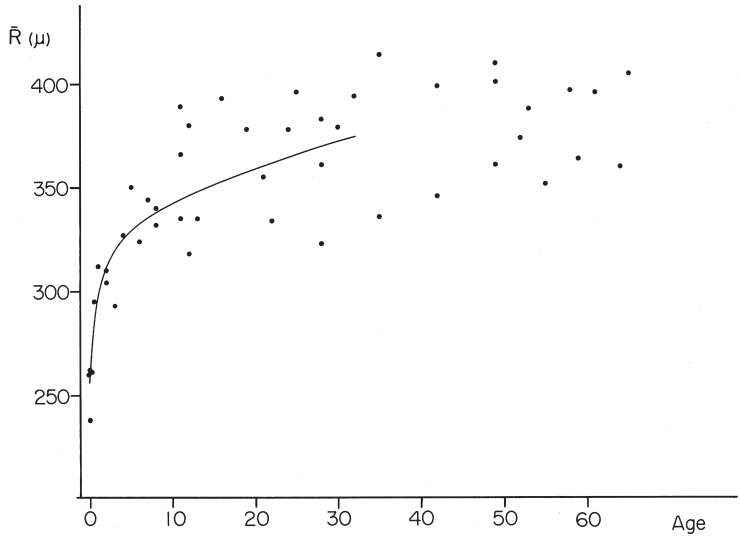

Fig. 2-39. The mean radius of hepatic lobule *R* estimated on 36 normal autopsy livers and plotted against the patients' age. This expresses the growth curve, not of the whole organ, but of hepatic parenchyma. Reproduced from Takahashi *et al*. (1968): Tohoku J exp Med 94, pp. 212.

chapter.

Hypertrophic lobules in livers harboring hepatocellular carcinoma (Fig. 2-40)

The measurement of *R* was extended to autopsy livers from eight patients, in whom the liver was demonstrated harboring hepatocellular carcinoma but development of tumor was considered unusual in that there was no foregoing cirrhosis or chronic hepatitis which usually is associated. As in Fig. 2-40, the estimated *R* appears much larger in the eight cases of liver carcinoma arising in non-cirrhotic livers than in the normal control; the mean *R* in the tumor group was 481.5 μm and the difference proved to be highly significant. It might seem possible that the enlarged *R* in the livers with hepatocellular carcinoma is an expression of compensatory hypertrophy, but this is untenable, seeing that in another series of livers harboring metastatic nodules of carcinoma originating from other organs, the mean *R* proved not to be significantly larger than the normal group. Thus it seems likely, as expected, that in the background of hepatocellular carcinogenesis, a sort of pathological growth of liver parenchyma is advancing.

Another application of L_V: proliferating bile ducts in livers with congenital bile duct atresia

Another application of the above relation (2-7) is found in the study of Oh-i *et al.* (1969) dealing with the changes of liver in infants with congenital biliary atresia. Infants having this disease are born with the extrahepatic bile ducts totally obstructed and replaced with scar-like cords. There had been little life-saving measure for this

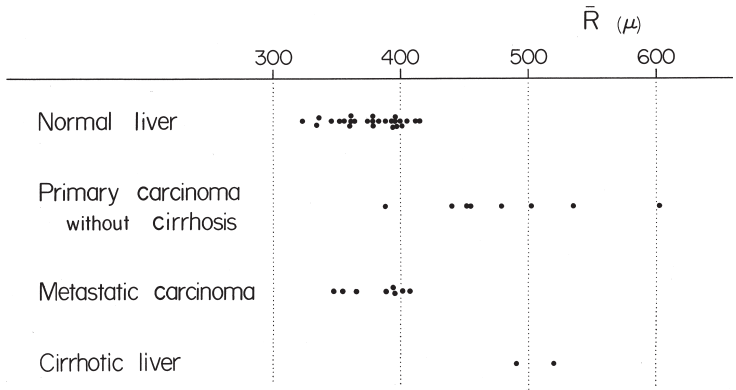

Fig. 2-40. The mean radius of hepatic lobule *R* is compared between normal adult livers and eight non-cirrhotic livers harboring hepatocellular carcinoma. The average *R* is significantly larger in the latter group, suggesting that a sort of pathological growth of liver parenchyma is progressing in the background of carcinoma development. Reproduced from Takahashi *et al*. (1968): Tohoku J exp Med 94, pp. 217.

disease until 1968, when Kasai *et al*. introduced a surgical treatment (hepatoenterostomy) which greatly extended surgical indication. However in the early days of trial, the result of operation was variable. It was known that the prognosis crucially depends upon the presurgical duration of jaundice, as shown by the fact that an operation, when performed on patients over four months of age, did not bring about any relief of jaundice. Microscopically, the livers of patients presented pictures consistent with biliary cirrhosis, but in those who were not relieved from jaundice, it was not known what changes were mainly to blame for bile-draining failure. In view of this, Oh-i *et al*. undertook a re-assessment of the changes, resorting to micromorphometry and 3-D reconstruction of small bile ducts. In thirty infants operated for congenital bile duct atresia, liver specimens were obtained at correction surgery or autopsy. The patients were divided into two groups: those in whom jaundice was reduced postoperatively (Group 1) and those in whom little change was confirmed (Group 2). The livers were submitted to measurement of two values: V_i, the volume density of interstitium, and L_V(ducts), the length density of bile ducts and ductules. V_i was obtained by chord length measurement to describe the grade of fibrosis. L_V(ducts), determined from the numerical density of ducts and ductules in a sample area (L_A) and applying the formula (2-7), served as an expression of ductal proliferation that was more or less found in the livers. In Group 2, both the mean V_i and L_V(ducts) proved to be significantly larger than in Group 1, showing that in Group 2 the livers had more advanced fibrosis, but there was also proliferation of bile ducts and ductules that was more vigorous than in Group 1. To examine whether the proliferating ducts form a continuous draining system, manual reconstruction of intrahepatic ducts was added from serial sections of selected livers. It was shown that the peripheral biliary system was replaced by an extremely complex network of proliferating ductules, which was interpreted as a reaction of biliary system to bile stagnation and leakage to the periportal

area. The restoration of patent intrahepatic bile system seemed to depend upon the preservation of pre-existing "main routes" of passage, and not on the grade of ductular proliferation. Thus the maintenance of anatomically recognizable routes of drainage was considered the crucial prerequisite for a successful correction operation.

h) Problems that cannot be solved by stereology

Classification of geometric properties of 3-D features (Table 2-2)

We have seen examples of studies to which principles of classic stereology were applied, but then, can we solve all problems of 3-D structures with stereology? So long as the biostructure is concerned, the applicability of stereology seems much more limited than it had been expected before. Table 2-2 is a classification of geometric properties given by DeHoff (1982) from such a viewpoint, and here, stereological estimation is shown workable in rather limited occasions. In addition, in the domain of pathologic anatomy where we have been working, quantitative analysis faces another difficulty. Application of stereology requires *uniform randomness* of the object in terms of distribution or orientation, while dealing with real organs one may often be hampered by the appearance of structure where the condition of randomness may scarcely be satisfied. Still, on such occasions, we are provided with two possibilities.

One is the extension of theoretical methods as have been proposed by European

Table 2-2. Classification of geometric properties according to whether stereology can effectively be applied. Reproduced from DeHoff (1983).

Class I:	Standard stereological properties, estimated without geometric assumptions.
	Volume fraction
	Area of surfaces or interfaces
	Length of lines, edges, or triple lines
	Integral mean curvature of surfaces
	Integral curvature of lines
	Integral torsion of lines
Class II:	Properties that require geometric assumptions for their estimation.
	Feature size distribution
	Number of features (simple shapes)
	Feature averages (volume, area, size)
	Degree of anisotropy
Class III:	Properties that cannot be estimated stereologically.
	Number of features (general)
	Connectivity of features (general)
	Size distributions (by volume, area, diameter)
	Spatial distribution information (covariograms)
	Real feature shape

researchers in various aspects of quantitative morphology, now generally called the new stereology. The fruit of their activity includes various new concepts which have been applied to granulometry (Gundersen, 1985; Gundersen *et al*., 1988) or measurement of non-randomized structure (Baddeley *et al*., 1985; Cruz-Orive *et al*., 1990). Sometimes we also have been assisted by these new tools. For example, Ebina *et al*. (1993) resorted to disector technique of Gundersen in his study dealing with the problem about whether hypertrophy or hyperplasia causes thickening of bronchial smooth muscles in asthmatic patients; here the number of cell nuclei (N_V) had to be determined.

The other approach is to attempt directly analyzing the 3-D space. Certainly, the 3-D structural analysis requires one to perform time and energy-consuming job like 3-D reconstruction from serial sections. However, it promises the performer to obtain fertile knowledge about the organ structure. Recently, we managed to bring into this field computer-assist, with which we have not only been aided to perform reconstruction at greatly improved speed and precision, but also managed to extend the scope of 3-D structural studies, for example into computational measurement of 3-D quantities. What we have done along this line will be the main theme of the chapters that follow.